Geoscience Frontiers 13 (2022) 101275

Contents lists available at ScienceDirect

Geoscience Frontiers

journal homepage: www.elsevier.com/locate/gsf

Research Paper

Terrestrial records of the early Albian Ocean Anoxic Event: Evidence from the Fuxin lacustrine basin, NE China

Xiao-Tao Xu [a,b], Long-Yi Shao [a,*], Kenneth A. Eriksson [c], Bo Pang [d], Shuai Wang [a], Cheng-Xue Yang [e], Hai-Hai Hou [f]

[a] College of Geoscience and Surveying Engineering, China University of Mining and Technology (Beijing), Beijing 100083, China
[b] Shandong Key Laboratory of Depositional Mineralization & Sedimentary Mineral, Shandong University of Science and Technology, Qingdao 266590, China
[c] Department of Geosciences, Virginia Tech, Blacksburg, VA 24061, USA
[d] Liaoning Province Geology and Minerals Group Energy Geology Co., Ltd., Shenyang 110000, China
[e] Institute of Earth Sciences, China University of Geosciences (Beijing), Beijing 100083, China
[f] College of Mining, Liaoning Technical University, Fuxin 123000, China

ARTICLE INFO

Article history:
Received 3 May 2021
Revised 7 July 2021
Accepted 21 July 2021
Available online 24 July 2021
Handling Editor: M. Santosh

Keywords:
Fuxin Basin
Early Albian
Organic carbon isotopes
Ocean Anoxic Event 1b
Terrestrial records

ABSTRACT

The early Albian Oceanic Anoxic Event 1b (OAE 1b) is well documented in the Tethys, Pacific and North Atlantic, but few studies have evaluated whether or not terrestrial records of OAE 1b exist. In order to identify terrestrial records of the early Albian OAE 1b and to infer possible driving mechanisms, an integrated multi-proxy study from the late Aptian to Albian in the Fuxin lacustrine basin was conducted, including thick, organic-rich black mudstones, total organic carbon (TOC), organic carbon isotopes ($\delta^{13}C_{org}$), mercury concentration (Hg) and results from pyrolysis analyses (S_2, T_{max} and HI). Results show three distinct short-term negative $\delta^{13}C_{org}$ excursions corresponding with relatively high TOC values, which could be counterparts of the Kilian, Paquier and Leenhardt sub-events of the early Albian OAE 1b. Atmospheric CO_2 concentration (pCO_2) recovered from C_3 plant $\delta^{13}C_{org}$ compositions indicates an increasing trend in Unit C during the early Albian, and there are three short-term increases of pCO_2 corresponding to the three sub-events of OAE 1b at this time interval. We infer that a trend of increasing pCO_2 during the Kilian sub-event in the study area is closely related to volcanism. Continental weathering calculated using chemical weathering indices (CIA, WIP and $MIA_{(O)}$) show an increasing trend during the OAE 1b interval, likely resulting from warmer and more humid conditions. Mixed sources of terrestrial plants and lacustrine plankton demonstrated by pyrolysis analyses (HI vs. T_{max} and S_2 vs. TOC), indicate a terrestrial contribution to the organic-rich sediments of the Kilian, Paquier and Leenhardt sub-events of OAE 1b. We suggest that a CO_2-forced greenhouse effect during the early Albian might have triggered the relatively warm and humid palaeoclimatic conditions, and intensified chemical weathering that combined to create high nutrient and organic matter levels that were flushed into lakes contributing to eutrophication and anoxia in lacustrine and in contemporaneous oceanic systems.

1. Introduction

"The Cretaceous World" (Skelton, 2003) was a complex time period in Earth's history with many important geological events, including Large Igneous Provinces (LIPs) (Coffin and Eldholm, 1994), rapid increases in ocean crust (Larson, 1991), Oceanic Anoxic Events (OAEs) (Schlanger and Jenkyns, 1976) and Cretaceous Oceanic Red Beds (CORBs) (Wang et al., 2005; Hu et al., 2006). OAEs proposed by Schlanger and Jenkyns (1976) have attracted widespread attention in geological research. Cretaceous multiple black mudstones and OAEs are considered to be an important window for understanding the carbon cycle in Earth's evolution (Wang, 2006). Cretaceous OAEs have been recognized for more than 40 years at both global and regional scales (e.g., Leckie et al., 2002; Jenkyns, 2010; Coccioni et al., 2014; Benamara et al., 2020). The duration (~20 m.y.) of Aptian-Albian OAE 1 is divided into four time intervals: OAE 1a (~120.5 Ma), 1b (~113–109 Ma), 1c (~102 Ma) and 1d (~99.5 Ma) (Bralower et al., 1999; Leckie et al., 2002). Moreover, OAE 1b is an interval spanning the Aptian/Albian boundary that contains several perturbations of the global carbon cycle and deposition of multiple black mudstone

* Corresponding author.
E-mail address: ShaoL@cumtb.edu.cn (L.-Y. Shao).

https://doi.org/10.1016/j.gsf.2021.101275
1674-9871/

intervals with relatively enhanced organic carbon contents (Trabucho Alexandre et al., 2011). According to a new, detailed stratigraphic discussion and redefinition of the OAE 1b proposed by Coccioni et al. (2014), OAE 1b is subdivided into four discrete sub-events: Jacob, Kilian, Paquier and Leenhardt sub-events delineated by four laminated organic-rich layers and synchronous perturbations in the carbon isotope records.

The multiple black mudstones of OAE 1b are relatively enriched in total organic carbon (TOC) (e.g., Bralower et al., 1999; Tsikos et al., 2004; Herrle et al., 2015). OAE 1b is widely distributed in the Tethys, Atlantic and Pacific Ocean Basins (Jenkyns, 2010; Sabatino et al., 2015; Benamara et al., 2020), and OAE 1b records have been reported from about twenty localities around the world (Fig. 1). Carbon isotope records can be used to establish global organic carbon budgets during the OAEs (Bralower et al., 1999), and distinct carbon isotopic excursion can be used as an important identifier of OAEs (Coccioni et al., 2014; Li et al., 2016). Global correlation of OAEs can be established by comparing the abnormal excursions of inorganic carbon isotope or organic carbon isotope in vertical section from different regions (Bralower et al., 1999; Sabatino et al., 2015). The four sub-events of OAE 1b record several perturbations of the global carbon cycle (Herrle et al., 2004; Sabatino et al., 2015), and there are distinct abnormal shifts in carbon isotope records during this period. The Kilian, Paquier and Leenhardt sub-events are characterized by particularly distinct negative shifts of carbon isotope values in the Vocontian Basin (Herrle et al., 2003, 2004; Friedrich et al., 2005; Coccioni et al., 2014). In contrast, the Jacob sub-event of OAE 1b is defined by a positive excursion in the carbon isotope record (Herrle et al., 2003; Herrle et al., 2004).

The driving mechanism of OAE 1b is still under dispute. According to existing models, possible causes of OAE 1b include intense volcanic activity (Wagner et al., 2007; Li et al., 2016), increased thermohaline stratification (Erbacher et al., 2001), accelerated hydrologic cycle linked to increased runoff, continental weathering, terrestrial input and surface water productivity (Leckie et al., 2002; Herrle et al., 2003; Jenkyns, 2010), enhanced monsoonal activity (Herrle et al., 2003; Benamara et al., 2020) and sea level changes (Erbachen et al., 1998; Leckie et al., 2002), either singularly or in combination.

The discovery of OAEs was originally based on the Deep Sea Drilling Project (Schlanger and Jenkyns, 1976) as part of the long-term research project on oceanic sediments. Large-scale burial of organic carbon caused by OAEs has a profound impact on the global atmosphere–ocean system (Huang et al., 2008; Gao et al., 2017) and, therefore, the global carbon cycle might have contained OAEs records in contemporaneous terrestrial sediments. Organic-rich black mudstones deposited in continental settings should be important OAEs records that are contemporaneous with marine records and which will provide significant supplements for a comprehensive understanding of OAEs. Lacustrine organic-rich horizons, coeval with their marine counterparts, might have developed during time intervals characterized by OAEs, which may explain some of the Cretaceous organic-rich sediments formed in the rift basins (Jenkyns, 2010). Further studies of Cretaceous OAEs have been extended to contemporaneous terrestrial

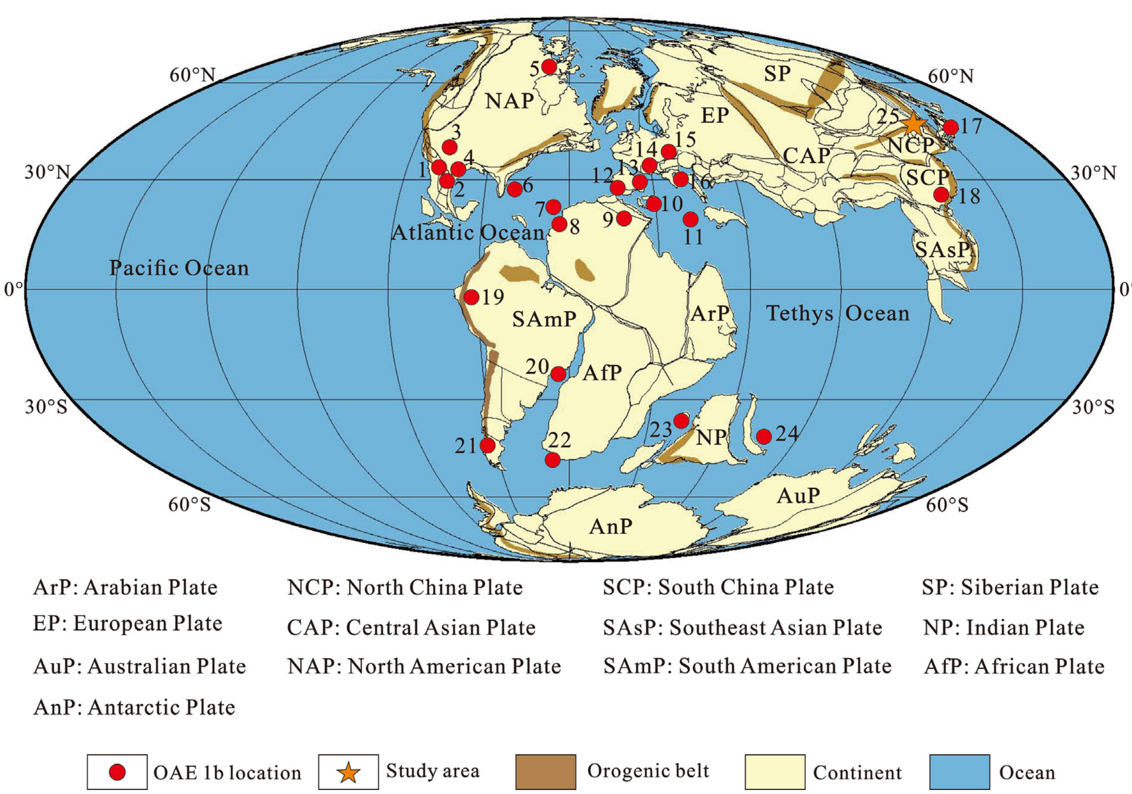

Fig. 1. Global palaeogeographic map of the Early Cretaceous (~120 Ma) (modified after Li and Jiang, 2013), showing approximate locations of main OAE 1b events and the inferred palaeolatitude position of the study area (Location 25). 1. North Sonora, NW Mexico; 2. Northeastern Mexico; 3. Price River, Utah, USA; 4. Northern Gulf of Mexico, southern Texas, USA; 5. Axel Heiberg Island in the Canadian Arctic; 6. ODP site 1049 off northern Florida, Blake Nose escarpment, western North Atlantic; 7. DSDP Site 545, Mazagan Plateau, eastern North Atlantic; 8. Essaouira-Agadir Basin, southern Morocco; 9. Northern Tunisia; 10. Umbria-Marche Basin, central Italy; 11. Zagros Mountains, SW Iran; 12. Aralar Platform, SE Basque-Cantabrian Basin, northern Spain; 13. Briançonnais Domain, a palaeogeographic unit in the Alps; 14. Vocontian Basin, SE France; 15. Helvetic platform, northern Tethyan margin; 16. Ionian Basin, NW Greece; 17. Hokkaido, Japan; 18. Zhejiang and Fujian provinces, SE China; 19. Andean Basin, northern Peru; 20. Campos Basin, SE Brazilian continental Margin; 21. Lago San Martin, southern Argentina; 22. DSDP Site 511, central Falkland Plateau, southern South Atlantic; 23. ODP Site 763, southwestern flank of Exmouth Plateau, southeast Indian Ocean; 24. Southern Tibet, China; 25. Fuxin Basin, NE China.

deposits (Ando and Kakegawa, 2007; Ludvigson et al., 2010; Hu et al., 2014; Gao et al., 2019; Xu et al., 2020a) and, in particular, to continental lacustrine basins. However, few studies have reported terrestrial records of OAEs. In this study, we conduct analyses of thick, organic-rich black mudstones, TOC, organic carbon isotope ($\delta^{13}C_{org}$) and mercury concentration (Hg) and results from pyrolysis analyses (S_2, T_{max} and HI), which provide the opportunity to explore changing trends of atmospheric CO_2 concentration (pCO_2) and palaeoclimate, and sources of organic matter during the early Albian OAE 1b. This study also attempts to explain the genesis of thick, organic-rich black mudstones in lakes. These results provide terrestrial records of the early Albian OAE 1b in northeastern China and make a contribution to the comprehensive understanding of OAE 1b.

2. Geological setting

The continental Fuxin Basin is located in the western Liaoning Province, northeastern China and is situated in the northern part of the eastern North China Plate (NCP), within a triangular area between the Tanlu and Chifeng-Kaiyuan faults (Fig. 2a; Wang et al., 1998; Zhu et al., 2007). During the Jurassic–Cretaceous, the eastern NCP was located in a back-arc setting with respect to subduction of the Palaeo-Pacific Plate (e.g., Zhu et al., 2017; Su et al., 2021). The Early Cretaceous represents a peak period of rifting and magmatism in the eastern NCP (Wu et al., 2014; Zhu et al., 2017). The Fuxin Basin is a faulted basin (Fig. 2b), formed as a result of rifting in the Late Jurassic to Early Cretaceous (Liu et al., 1992; Wang et al., 1998), with a palaeolatitude of ~40–45°N during the Early Cretaceous (Zhou et al., 2003; Li and Jiang, 2013). It is bounded by the Lvshan Fault to the east and the Songling Fault to the west, with both faults being NNE-trending (Liu and Chen, 1995), and extends from the Shala city in the north to the Dalinghe Fault in the south (Fig. 2c).

The Fuxin Basin overlies Archean and Middle Proterozoic basement and contains Cretaceous and Cenozoic strata. From the oldest to the youngest, the Lower Cretaceous strata of the Fuxin Basin are composed of the Yixian, Jiufotang, Shahai, Fuxin, and Sunjiawan formations (National Commission on Stratigraphy of China, 2014). In this study, the Shahai and Fuxin formations were selected to identify terrestrial records of the early Albian OAE 1b and to infer its possible driving mechanisms. The Shahai Formation mainly consists of conglomerates, sandstones and mudstones, with minor coal seams, and has a maximum thickness of 1600 m (Zhang et al., 2005) with a depositional rate of ~152.9 m/Ma (Ma et al., 2000), which can be subdivided into the first, second, third and fourth members (Fig. 3). The Fuxin Formation is about

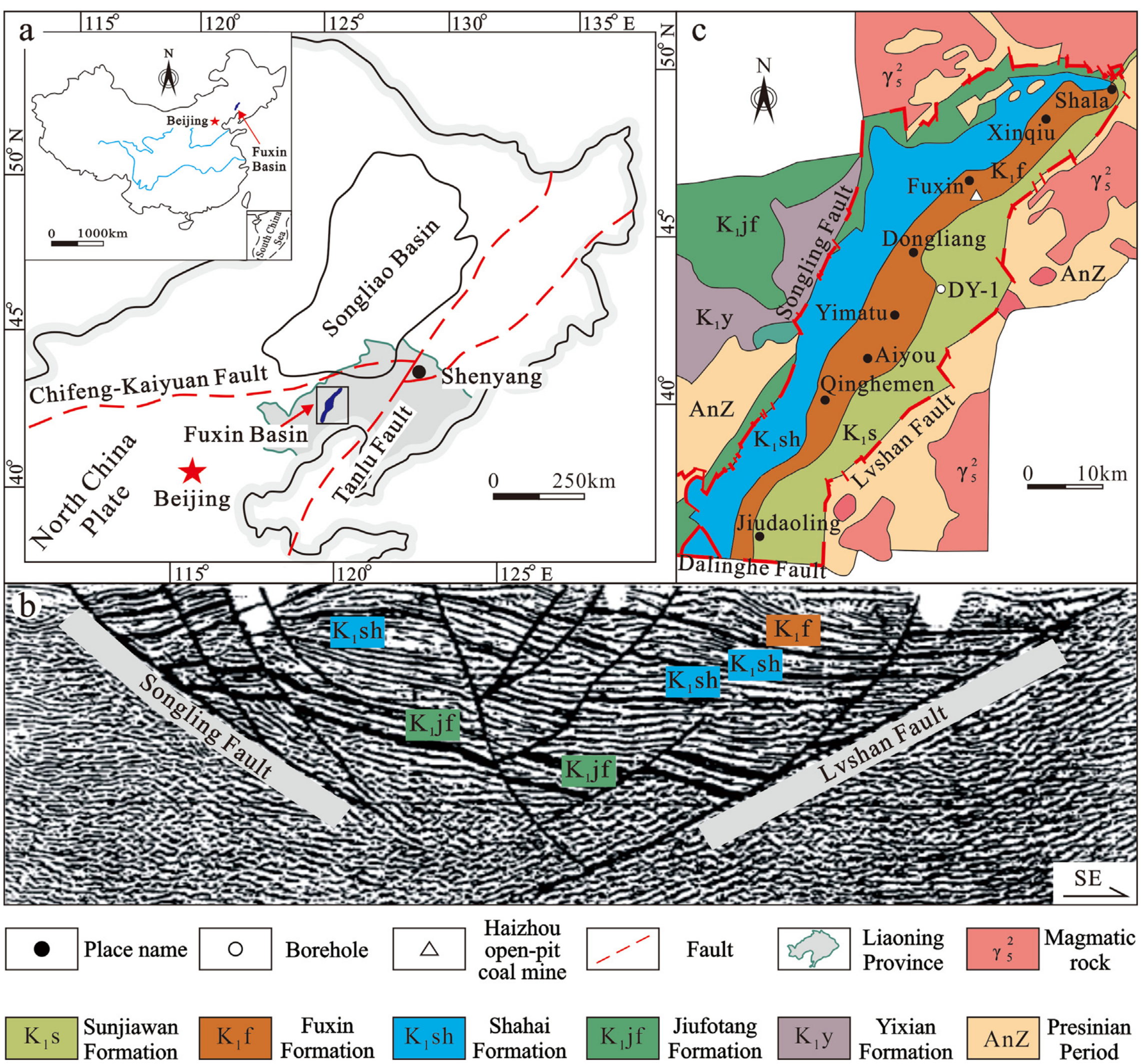

Fig. 2. (a) Location map of the Fuxin Basin (modified after Wang et al., 1998; Zhu et al., 2007). (b) NW-SE-trending seismic profile across the Fuxin Basin (modified after Wang et al., 1998). (c) Geologic map of the Fuxin Basin (modified after Sun, 2006).

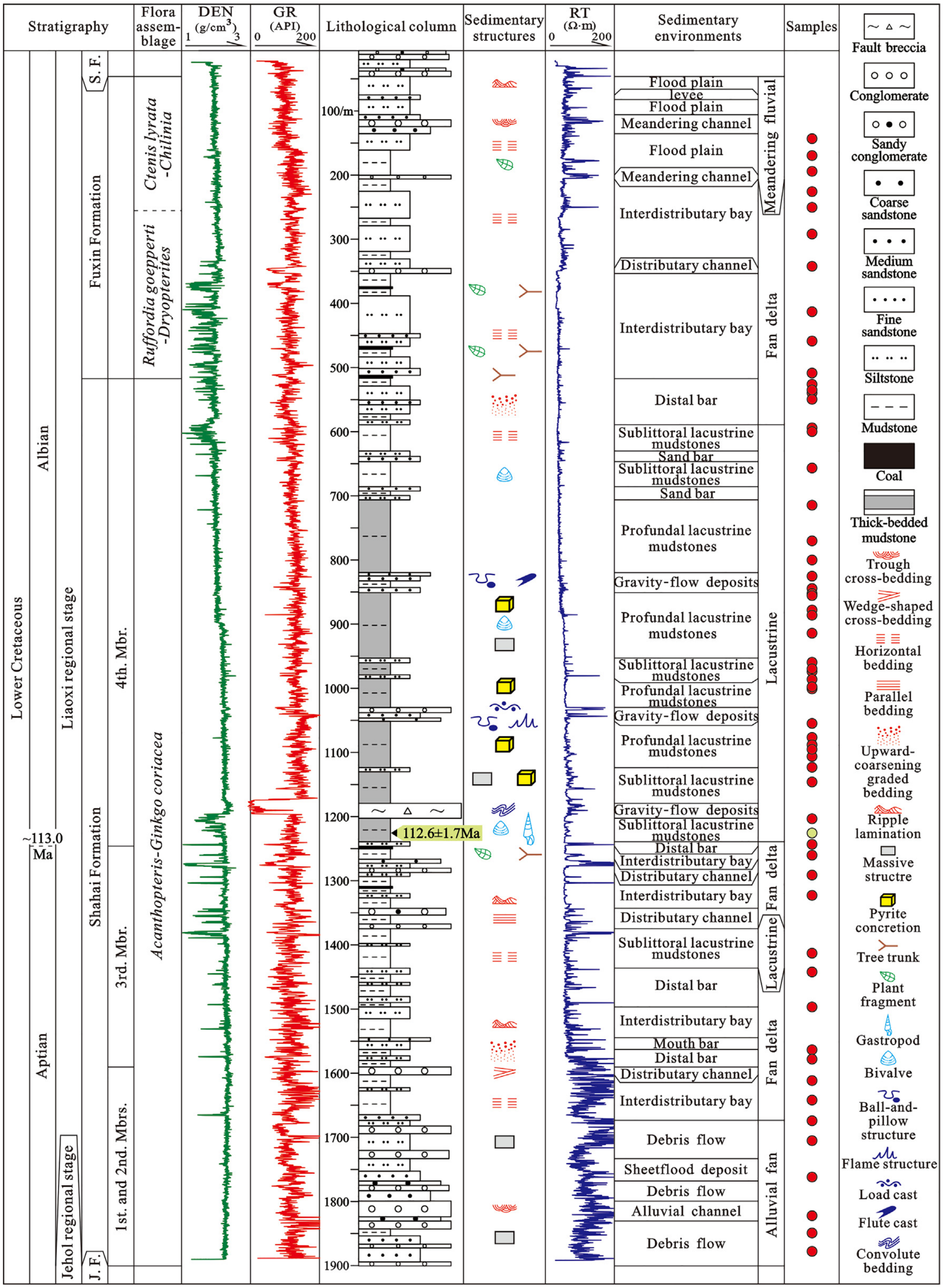

Fig. 3. Stratigraphic column of borehole DY-1 showing sedimentary facies and sample locations of the Shahai and Fuxin formations in Fuxin Basin (Borehole DY-1: see Fig. 2c for location). Zircon U-Pb dating of the tuffaceous claystone sample DY-1G near the bottom of the fourth member of the Shahai Formation (1225.5 m) gave an age of 112.6 ± 1.7 Ma. Abbreviations: J. F. = Jiufotang Formation; S. F. = Sunjiawan Formation; DEN = Density; GR = Gamma Ray; RT = Resistivity.

445–1100 m thick with a depositional rate of ~179.1 m/Ma (Ma et al., 2000), and is predominantly composed of sandstone and mudstone, with coal seam (Xu et al., 2020b). Available ages suggest the total depositional ages of ~12 Ma for the Shahai and Fuxin formations (Su et al., 2021).

The Lower Cretaceous is subdivided into the Jibei, Jehol and Liaoxi regional stratigraphic stages (Wan et al., 2013). Among these, the Liaoxi regional stage includes the Shahai, Fuxin and Sunjiawan formations from the bottom to the top (Fig. 3), and contains the Fuxin flora. The Fuxin flora is characterized by a dominance of ferns, Ginkgoales and conifers, with abundant Cycads and Equisetales. This flora can be subdivided into three distinct assemblages, comprising in the Shahai Formation the *Acanthopteris-Ginkgo coriacea* assemblage, in the lower-middle part of the Fuxin Formation the *Ruffordia goepperti-Dryopterites* assemblage, and in the upper part of the Fuxin Formation the *Ctenis lyrata-Chilinia assemblage* (Deng et al., 2012). The ages of these three assemblages are Early Cretaceous (Chen et al., 1988; Deng and Chen, 2001), and the Shahai and Fuxin formations date to the late Aptian to Albian ages (Deng et al., 2012; Xi et al., 2019).

3. Methods

Borehole DY-1 (41° 52′ 45″ N–121° 37′ 8″ E) is located in the central part of the Fuxin Basin, near Dongliang City (Fig. 2c). A total of 58 mudstone samples were collected from the bottom to the top of the Shahai and Fuxin formations (Fig. 3). For each sample, 300 g was collected and retained in air tight, zip-lock plastic bags. Every mudstone sample was milled into 200 mesh and divided into four parts for: (1) $\delta^{13}C_{org}$ analysis, (2) TOC analysis, (3) Hg concentration analysis, (4) S_2, T_{max} and HI analyses. In addition, one tuffaceous claystone sample DY-1G near the bottom of the fourth member of the Shahai Formation was collected for zircon U-Pb dating (Figs. 3 and 4a).

Zircon grains were extracted from the tuffaceous claystone and U-Pb dating was conducted by Laser ablation-inductively coupled plasma-mass spectrometry (LA-ICP-MS) at the State Key Laboratory of Geological Processes and Mineral Resources, China University of Geosciences, Beijing. Zircon 91500 was used as an external standard for U-Th-Pb isotopic ratios (Wiedenbeck et al., 1995; Wiedenbeck et al., 2004). Meanwhile, zircon Plešovice was used as a monitoring standard for each analysis (Sláma et al., 2008).

For $\delta^{13}C_{org}$ and TOC content analyses, mudstone samples milled to 200 mesh were first treated with dilute hydrochloric acid at 60–80 °C to remove inorganic carbon. Subsequently, insoluble residues were washed with distilled water to neutralize and then dried in an oven at 60–80 °C. $\delta^{13}C_{org}$ and TOC were measured at the Analytical Laboratory of the Beijing Research Institute of Uranium Geology. $\delta^{13}C_{org}$ was analyzed using a MAT-253 gas isotope mass spectrometer (8633) following GB/T 18340.2-2010 guidelines. Organic isotope ratios are reported in the $\delta^{13}C_{org}$ notation as per mil (‰) deviation relative to Vienna Pee Dee Belemnite standard (VPDB), with the absolute analysis error of ±0.1‰. TOC values were measured using a CS580A carbon–sulfur analyzer (11022) following the HJ 695-2014 standard, with the lower detection limits of 100 μg/g and the absolute analysis error of ±0.2%. Mercury concentrations were measured at the State Key Laboratory Coal Resources and Safe Mining (Beijing). Mercury concentrations were determined using a Lumex RA-915+ mercury analyzer according to China's national standard (GB/T 22105.1-2008).

Pyrolysis analyses were determined at the State Key Laboratory of Petroleum Resources and Prospecting, China University of Petroleum, Beijing, using an OGE-II instrument following the Method of Rock Pyrolysis Analysis (GB/T18602-2012). Samples were heated to 600 °C in a helium atmosphere to obtain S_2 and T_{max} (Espitalié et al., 1977). S_2 arises during progressive heating from 300 °C to 600 °C, and T_{max} represents the temperature at maximum of the S_2 peak (Espitalié et al., 1977). Hydrogen index ($HI = S_2 \times 100/TOC$) is calculated from the pyrolysis analysis data and TOC values (Pepper and Corvi, 1995).

4. Results

4.1. U-Pb zircon ages data

Twenty zircon grains from tuffaceous claystone sample DY-1G near the bottom of the fourth member of the Shahai Formation were selected for dating using LA-ICP-MS. Cathodoluminescence (CL) images demonstrate that zircons from the tuffaceous claystone sample have euhedral morphologies and clear oscillatory zoning (Fig. 5a), suggesting a magmatic origin. Moreover, the Th/U ratios are between 0.59 and 2.37, which are similar to magmatic zircons (e.g., Zhu et al., 2013). $^{206}Pb/^{238}U$ dating results for the sample are shown in Fig. 5 and Table 1. Analysis of the 20 zircon grains from the tuffaceous claystone shows near-concordant $^{206}Pb/^{238}U$ ages ranging from 107.7 ± 4.0 Ma to 122.3 ± 4.3 Ma, with a weighted mean age of 112.6 ± 1.7 Ma (MSWD = 1.2, N = 20) (Fig. 5b). This age constrains the lower part of the fourth member of the Shahai Formation to the early Albian.

4.2. Depositional systems

The depositional systems of Shahai and Fuxin formations in the Fuxin Basin were investigated based on data from outcrop sections (Fig. 2c) and borehole cores (Fig. 6). Five major lithological types were identified, including conglomerates, sandstones, siltstones, mudstones and coals. Sedimentary environments in Shahai and Fuxin formations are interpreted as forming in a continental basin setting, including alluvial fan, braided fluvial, meandering fluvial, fan delta, and lacustrine depositional systems. The main characteristics of these depositional systems are summarized below.

4.2.1. Alluvial fan depositional system

The alluvial fan depositional system is mainly developed in the first and second members of the Shahai Formation and in the Fuxin Formation in the basin margins. It mainly comprises conglomerates, sandy conglomerates, and coarse-grained sandstones. Lenticular, massive, and grain-supported conglomerate deposits are generally moderately sorted and clasts are subangular to subrounded (Fig. 4b). Conglomerate beds with trough cross-bedding and scoured bases are interpreted as alluvial channel deposits. Poorly sorted, subangular and matrix-supported, massive conglomerate deposits are interpreted as products of debris flows on an alluvial fan (Figs. 4c and 7a). Planar cross-bedded medium-grained sandstone deposits interbedded with siltstone and mudstone are moderately sorted and subangular to subrounded, are related to sheetfloods on alluvial fans.

4.2.2. Braided fluvial depositional system

Five major lithological types including conglomerate, sandstone, siltstone, mudstone and coal are identified in the braided fluvial depositional system, which is characterized by cylindrical-shaped gamma ray and apparent resistivity logging curves. This depositional system is represented in the upper part of the Fuxin Formation towards the basinward areas. Lateral discontinuity of grain-supported conglomerate and conglomeratic sandstone deposits with trough cross-bedding coupled with scoured bases are suggestive of channel deposits in a braided fluvial setting (Fig. 7b). Sheet-like to lenticular and planar cross-bedding medium-grained sandstones indicate channel bar deposits (Fig. 7c), which are similar to the deposits of longitudinal bars described by Miall (2010). The sheet-like siltstone and mudstone with ripple lamination and horizontal bedding suggest reworking of previously deposited flood plain sediments. Massive carbonaceous mudstones and coal with plant fossils also resemble flood plain deposits.

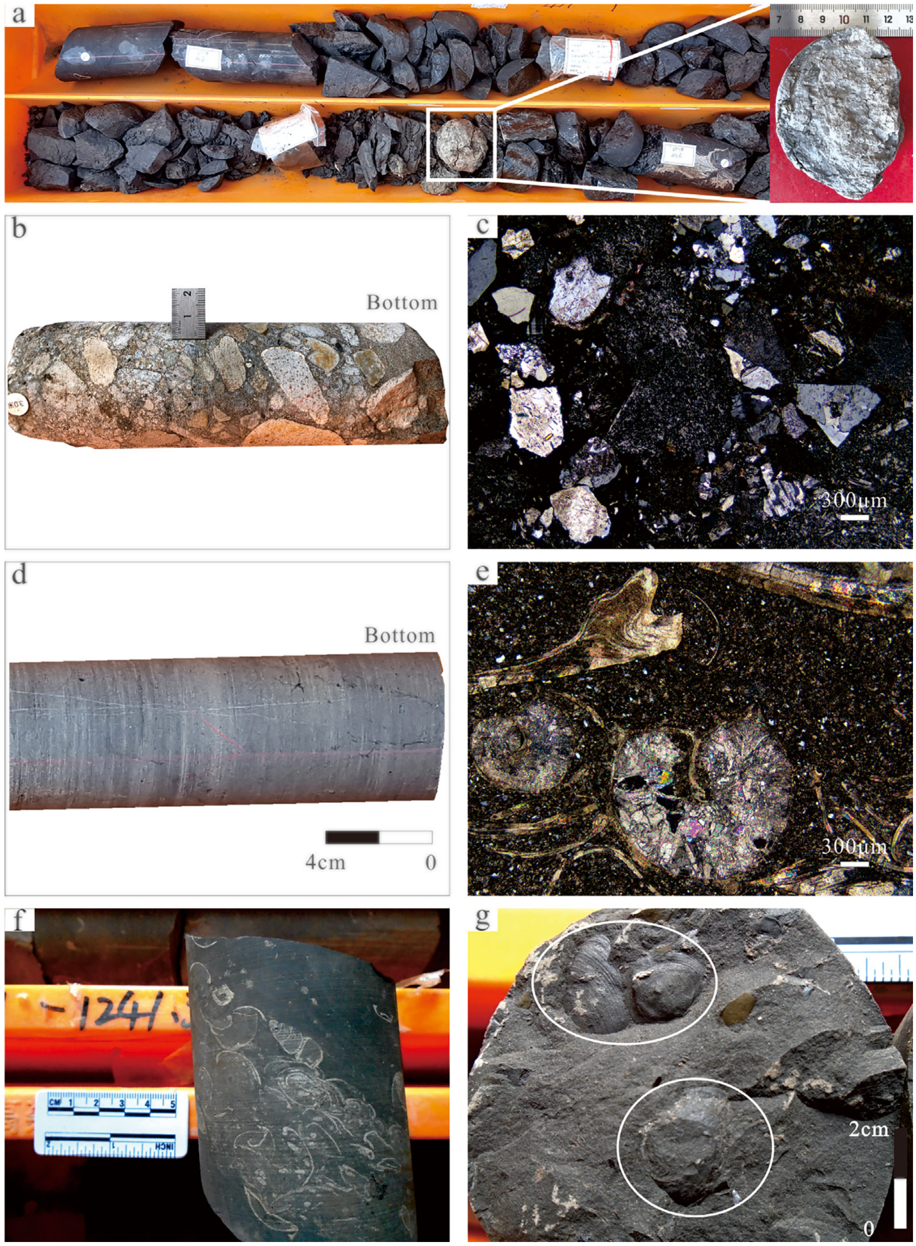

Fig. 4. Photographs of the Shahai and Fuxin formations in the Fuxin Basin from borehole DY-1. Depth locations are shown in Fig. 3. (a) Tuffaceous claystone, Shahai Formation, 1225.5 m. (b) Massive grain-supported conglomerate; first and second members of Shahai Formation, 1813.5 m. (c) Photomicrograph of poorly-sorted, matrix-supported conglomerate with subangular clasts; first and second members of Shahai Formation, 1880.35. (d) Horizontally bedded siltstone interbedded with mudstone; third member of Shahai Formation, 1543.61 m. (e) Photomicrograph of fossil fragments of gastropods and bivalves; fourth member of Shahai Formation, 1241.9 m. (f) Black mudstone with fossil fragments of gastropods and bivalves; fourth member of Shahai Formation, 1235 m. (g) Dark grey mudstone containing bivalve fossils; fourth member of Shahai Formation, 1234.5 m.

4.2.3. Meandering fluvial depositional system

Compared with the braided fluvial depositional system, the meandering fluvial system is characterized by upward-fining successions, mainly consisting of meandering channel, overbank, and flood basin deposits. The meandering fluvial depositional system was mainly found in the upper part of the Fuxin Formation. The conglomerate interbedded with coarse-grained sandstone with scoured bases suggests meandering channel deposition (Fig. 7d). The overbank is composed of crevasse splay and levee deposits and typically characterized by ripple laminated fine-grained sandstone (Fig. 7d) and wedge-shaped and climbing ripple cross-bedded siltstone interbedded with mudstone (Fig. 7e) and plant fossils (Fig. 7f). The sheet-like siltstone with ripple lamination and horizontal bedding, horizontally bedded mudstone, massive carbonaceous mudstone, and thin- to medium-bedded coal demonstrate a flood plain, and the occurrence of root traces is common in this deposit.

4.2.4. Fan delta depositional system

The fan delta is dominated by distributary channel and interdistributary bay deposits. It is represented in the third member of the Shahai Formation and the Fuxin Formation. Lenticular, medium- to coarse-grained sandstone with wedge-shaped cross-bedding and scoured bases (Fig. 7g) indicates a distributary channel deposit. Overlying successions composed of siltstone containing ripple lamination and horizontally bedded siltstone interbedded with mud-

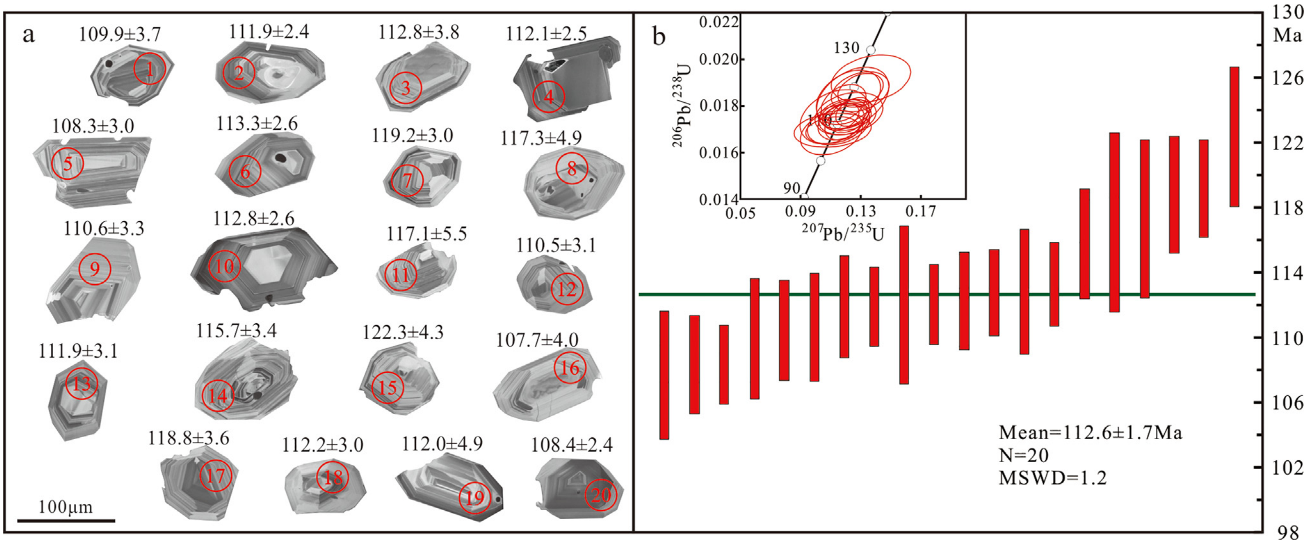

Fig. 5. (a) Cathodoluminescence (CL) images showing the internal structures of zircons from the tuffaceous claystone sample DY-1G near the bottom of the fourth member of Shahai Formation (DY-1, 1225.5 m). The red circles indicate laser ablation spots of LA-ICP-MS U-Pb dating. Ages are quoted in Ma. (b) Zircon U-Pb concordia plot and weighted mean age of tuffaceous claystone sample DY-1G. Vertical bars represent the ^{206}Pb/^{238}U zircon dates with 1 standard deviation. Abbreviations: MSWD = mean square of weighted deviations.

Table 1
Zircon U-Pb data for tuffaceous claystone sample DY-1G.

Spot	Th232	U238	Th/U	^{207}Pb/^{235}U	^{207}Pb/^{235}U	^{206}Pb/^{238}U	^{206}Pb/^{238}U	rho	^{206}Pb/^{238}U	^{206}Pb/^{238}U	Concordance
	ppm	ppm		Ratio	1sigma	Ratio	1sigma		Age (Ma)	1sigma	
DY-1G-1	229.0	180.8	1.27	0.1153	0.0137	0.0172	0.0006	0.2857	109.9	3.7	99%
DY-1G-2	233.8	192.3	1.22	0.1208	0.0107	0.0175	0.0004	0.2467	111.9	2.4	96%
DY-1G-3	144.5	147.4	0.98	0.1223	0.0149	0.0177	0.0006	0.2799	112.8	3.8	96%
DY-1G-4	283.8	234.6	1.21	0.1173	0.0077	0.0175	0.0004	0.3371	112.1	2.5	99%
DY-1G-5	125.4	135.0	0.93	0.1114	0.0169	0.0169	0.0005	0.1864	108.3	3.0	98%
DY-1G-6	230.4	201.8	1.14	0.1253	0.0078	0.0177	0.0004	0.3703	113.3	2.6	94%
DY-1G-7	169.5	151.2	1.12	0.1300	0.0100	0.0187	0.0005	0.3322	119.2	3.0	96%
DY-1G-8	219.5	189.5	1.16	0.1219	0.0141	0.0184	0.0008	0.3604	117.3	4.9	99%
DY-1G-9	193.0	134.8	1.43	0.1188	0.0113	0.0173	0.0005	0.3172	110.6	3.3	97%
DY-1G-10	157.6	267.9	0.59	0.1185	0.0104	0.0176	0.0004	0.2704	112.8	2.6	99%
DY-1G-11	237.9	198.7	1.20	0.1249	0.0159	0.0183	0.0009	0.3750	117.1	5.5	97%
DY-1G-12	225.3	197.8	1.14	0.1192	0.0086	0.0173	0.0005	0.3904	110.5	3.1	96%
DY-1G-13	312.0	254.8	1.22	0.1214	0.0126	0.0175	0.0005	0.2721	111.9	3.1	96%
DY-1G-14	188.4	183.7	1.03	0.1188	0.0098	0.0181	0.0005	0.3557	115.7	3.4	98%
DY-1G-15	497.5	271.8	1.83	0.1369	0.0175	0.0192	0.0007	0.2773	122.3	4.3	93%
DY-1G-16	190.1	178.6	1.06	0.1106	0.0137	0.0168	0.0006	0.3007	107.7	4.0	98%
DY-1G-17	415.6	228.9	1.82	0.1297	0.0128	0.0186	0.0006	0.3094	118.8	3.6	95%
DY-1G-18	358.1	263.3	1.36	0.1224	0.0089	0.0176	0.0005	0.3731	112.2	3.0	95%
DY-1G-19	142.9	122.5	1.17	0.1128	0.0153	0.0175	0.0008	0.3231	112.0	4.9	96%
DY-1G-20	899.5	379.4	2.37	0.1114	0.0119	0.0170	0.0004	0.2117	108.4	2.4	98%

stone (Fig. 4d) and plant fossils are interpreted as interdistributary bay deposits. The fan delta front comprises mouth bar and distal bar deposits. The upward-coarsening graded bedded and fine- to medium-grained sandstone with plant fossils is dark grey, moderately sorted, and subrounded, which resembles the mouth bar of fan delta. The sheet-like and horizontally bedded mudstone interbedded with siltstone suggests a distal bar deposit.

4.2.5. Lacustrine depositional system

The lacustrine depositional system is represented by dark grey siltstone, fine-grained sandstone and thick-bedded mudstone, which consists of littoral-sublittoral and profundal lacustrine deposits. This depositional system is characterized by a funnel-shaped and low-amplitude zig-zag-shaped logging curve. The well-sorted and well-rounded sandstones with rhythmic bedding and gastropod and bivalve fossils (Figs. 4e, 4f, 4g and 8a) demonstrate a littoral-sublittoral lacustrine setting. The sheet-like and horizontally bedded siltstones interbedded with fine- to medium-grained sandstones are interpreted as sand bars of littoral-sublittoral lacustrine deposits (Fig. 7h). Moreover, the sheet-like mudstones with horizontal bedding suggest deposition in a sublittoral lacustrine setting. Black and medium- to thick-bedded mudstones with massive bedding (Fig. 8b) represent profundal lacustrine deposits. Transported tree trunk fossils (Fig. 8c), organic-rich lamina in mudstone (Fig. 8d) and terrestrial plant fragments in organic-rich lamina (Fig. 8e) were also identified in the profundal lacustrine depositional system. The lacustrine depositional system is developed mainly in the fourth member of the Shahai Formation. In the DY-1 borehole core, a large number of fossil fragments of gastropods and bivalves are identified in lacustrine sedimentary facies at the base of the fourth member of the the Shahai Formation (Figs. 3, 4e, 4f, 4g and 8a). Based on an analysis of a NW-SE cross section of the fourth member of Shahai Formation, three, thick-bedded black mudstone intervals of lacustrine origin

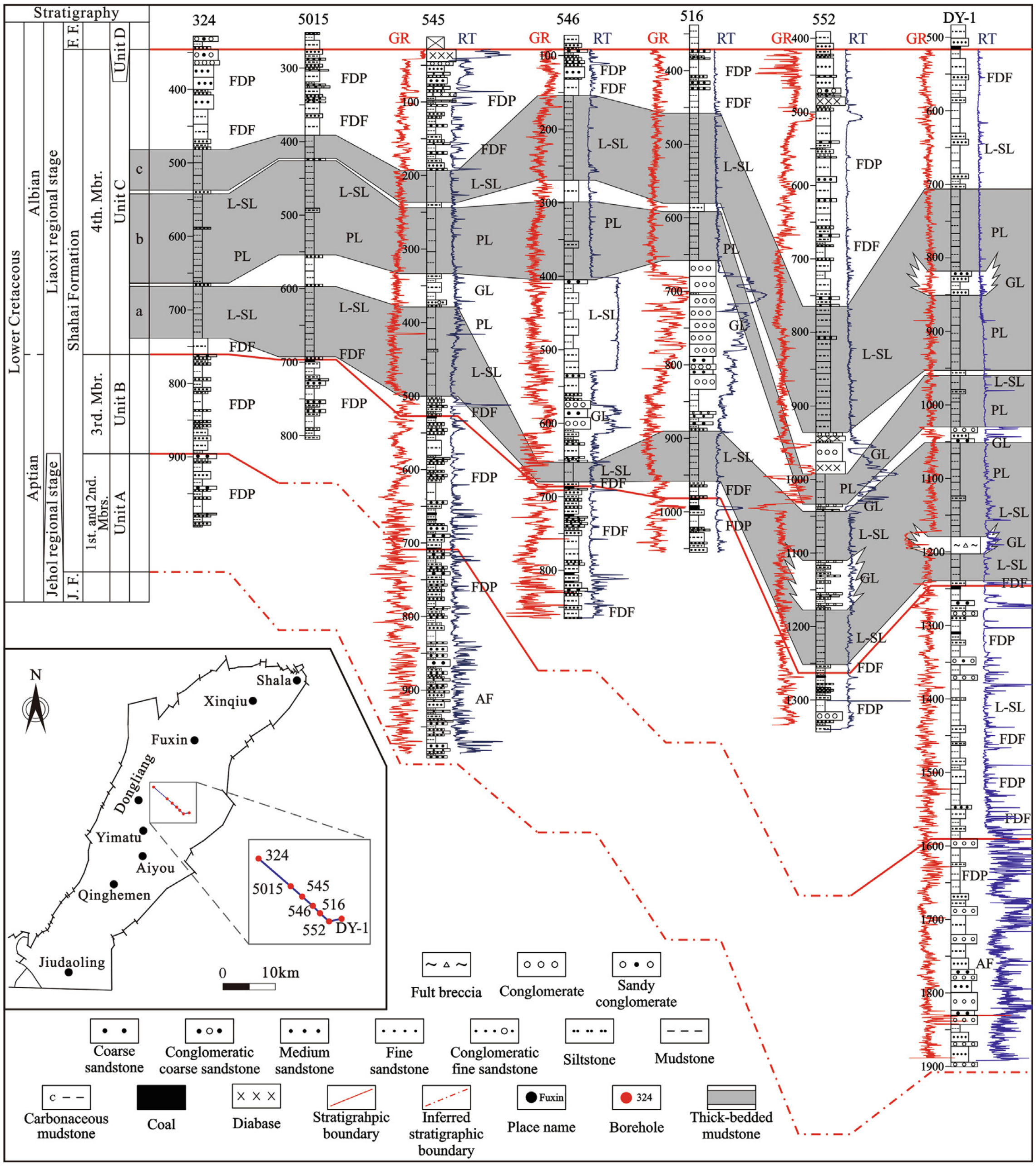

Fig. 6. NW-SE cross section showing sedimentary facies and distribution of thick-bedded mudstones from the Lower Cretaceous Shahai Formation in the Fuxin Basin. Three, thick-bedded black mudstone intervals of lacustrine origin (a, b and c) can be identified in the lower and middle parts of the fourth member of the Shahai Formation. Abbreviations: J. F. = Jiufotang Formation; F. F. = Fuxin Formation; AF = Alluvial Fan; FDP = Fan Delta Plain; FDF = Fan Delta Front; L-SL = Littoral-Sublittoral Lacustrine; PL = Profundal Lacustrine; GF = Gravity Flow; GR = Gamma Ray; RT = Resistivity.

(a, b and c) can be identified in the lower and middle parts of the fourth member of the formation (Fig. 6), which are mainly distributed in Dongliang area of the central part of Fuxin Basin. Thick-bedded black mudstones in the lower part (a) and the upper part (c) of the fourth member of Shahai Formation mainly developed in a littoral-sublittoral lacustrine depositional system, while the thick-bedded black mudstones in the middle part of the Shahai Formation (b) mainly developed in a littoral-sublittoral and deep, profundal lacustrine depositional system.

4.3. $\delta^{13}C_{org}$, TOC and Hg values

The results of $\delta^{13}C_{org}$, TOC and Hg values for 58 mudstone samples are given in Supplementary Data, Table S1 and Fig. 9. To simplify discussion and interpretation of the results, the study interval is subdivided into four units. Unit A developed during the early part of the late Aptian incorporates the first and second members of the Shahai Formation and is characterized by $\delta^{13}C_{org}$ values of high amplitude from −24.9‰ to −22.5‰ and TOC values from 0.84% to 2.08%. Unit B developed during the latest Aptian represents the third member of the Shahai Formation and has $\delta^{13}C_{org}$ values that range from −22.7‰ to −21.4‰ and TOC values of high amplitude ranging from 0.32% to 1.92%. Unit C developed during the early Albian defines the fourth member of the the Shahai Formation and is characterized by a prominent negative excursion in $\delta^{13}C_{org}$ with values ranging from −27.0‰ to −20.7‰ and with TOC values ranging from 0.57% to 4.76%. In Unit C, Hg concentrations vary from 1.17 to 131.80 ppb and Hg/TOC ratios vary from

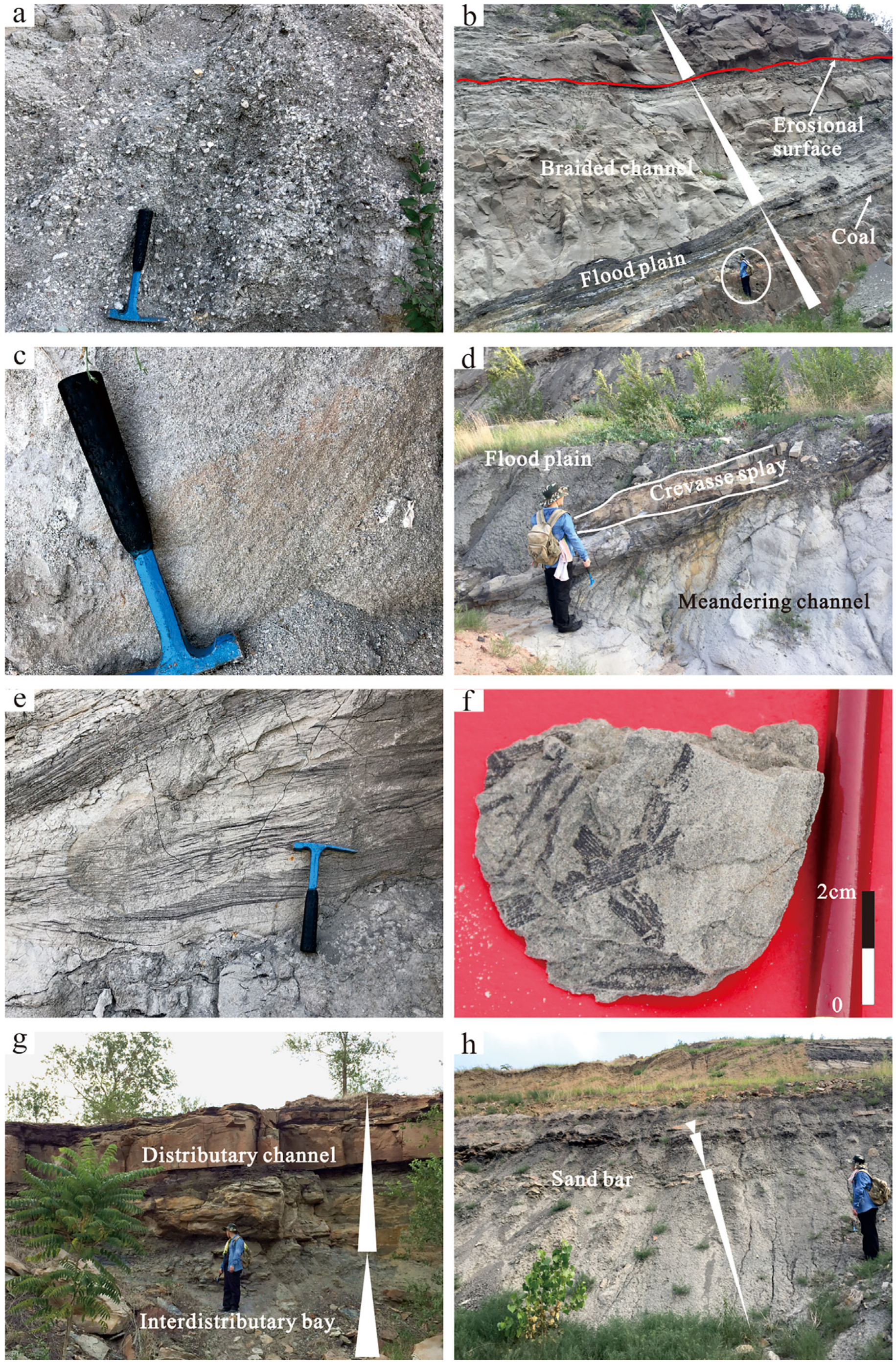

Fig. 7. Typical depositional systems of the Shahai and Fuxin formations in Fuxin Basin from outcrops. (a) Massive, matrix-supported conglomerate; alluvial fan depositional system, Haizhou open-pit coal mine section; the hammer is 30 cm long. (b) Massive conglomerate with horizontally bedded mudstone and tabular coal bed; braided fluvial depositional system, Haizhou open-pit coal mine section; the geologist is 173 cm tall. (c) Planar, cross-bedded, medium-grained sandstone; channel bar deposit, Haizhou open-pit coal mine section; the hammer is 30 cm long. (d) Horizontally bedded siltstone interbedded with mudstone and sheet-like coal, and small-scale, ripple laminated and fine-grained sandstone; meandering fluvial depositional system, Haizhou open-pit coal mine section; the geologist is 173 cm tall. (e) Climbing ripple, cross-laminated siltstone interbedded with mudstone; levee deposit, Haizhou open-pit coal mine section; the hammer is 30 cm long. (f) Grey siltstone with plant fossil fragments, Haizhou open-pit coal mine section. (g) Small-scale, wedge-shaped cross-bedding in medium- to coarse-grained sandstone with ripple cross laminated siltstone and horizontally bedded siltstone; fan delta depositional system, Haizhou open-pit coal mine section; the geologist is 173 cm tall. (h) Rhythmically bedded sandstone interbedded with siltstone, and horizontally bedded mudstone; sand bar deposit, Haizhou open-pit coal mine section; the geologist is 173 cm tall.

2.06 ppb/% to 27.69 ppb/%. $\delta^{13}C_{org}$ values of Unit C are lower than those of the other three units, and there are three sharp, short-term negative shifts during Unit C (Fig. 9; events I, II and III). Event I is the strongest negative excursion with a $\delta^{13}C_{org}$ peak value of -27‰ and occurs just at 1095.5 m. The obvious peaks in Hg/TOC ratio and Hg concentration all correspond to the peak of the strongest negative $\delta^{13}C_{org}$ excursion of event I. Event II is a weak negative $\delta^{13}C_{org}$ excursion with a $\delta^{13}C_{org}$ peak value of -26.2‰ and occurs at a depth of 974 m. Event III is a relatively weak negative excursion with a $\delta^{13}C_{org}$ peak value of -26.6‰ and occurs at a depth of 856 m. TOC values of Unit C are higher than those of the other units and the three sharp, short-term negative $\delta^{13}C_{org}$

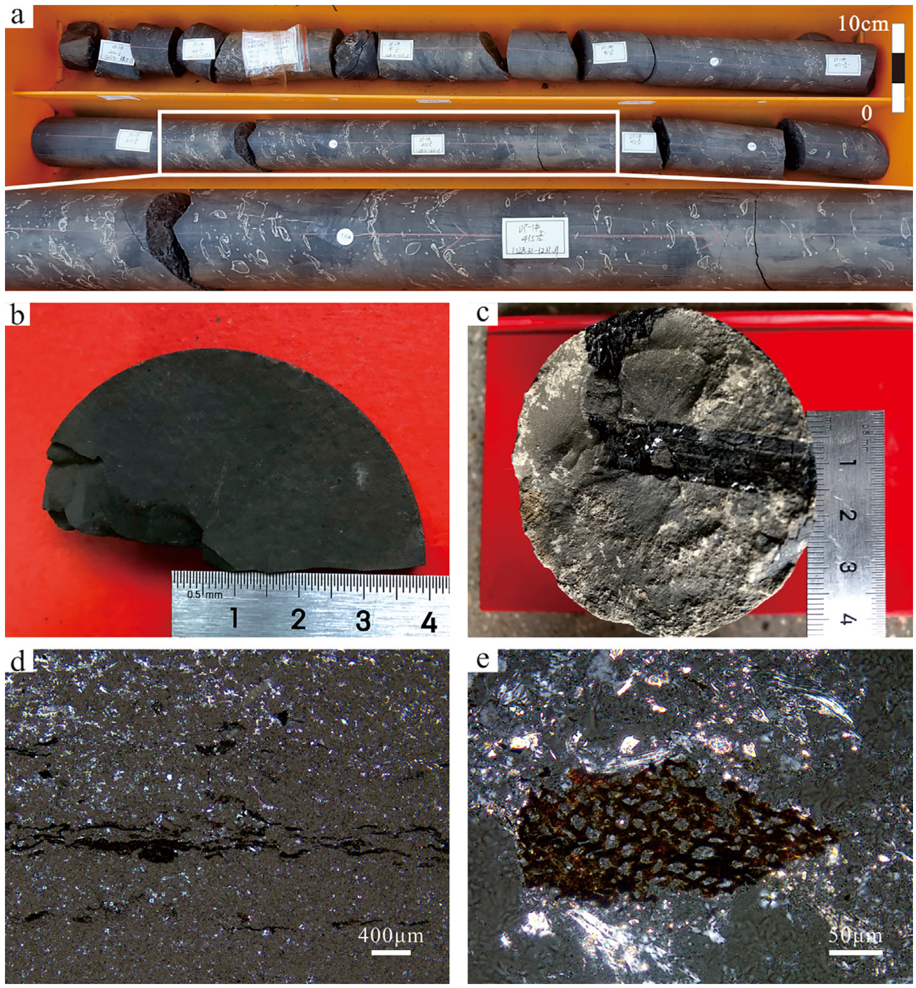

Fig. 8. Photographs of the Shahai and Fuxin formations in the Fuxin Basin from borehole DY-1. Depth locations are shown in Fig. 3. (a) Fossil fragments of gastropods and bivalves preserved in black mudstone; fourth member of the Shahai Formation, 1227.91–1229.91 m depth. (b) Massive black mudstone; fourth member of the Shahai Formation, 800 m depth, scale in cm. (c) Dark grey mudstone with tree trunk fossil; fourth member of the Shahai Formation, 834.7 m depth, scale in cm. (d) Photomicrograph of organic-rich laminae in mudstone; fourth member of the Shahai Formation, 946.3 m depth. (e) Photomicrograph of terrestrial plant fragments in organic-rich lamina; fourth member of the Shahai Formation, 946.3 m depth.

shifts all correspond to high TOC values. From the bottom to the top, TOC peak values of events I, II and III are 4.76%, 3.55% and 4.05%, respectively. Unit D developed during the middle and late Albian defines the Fuxin Formation and is characterized by $\delta^{13}C_{org}$ values that increase from −23.2‰ to −20.1‰; TOC values from 0.05% to 2.75% have a downward trend (Fig. 9).

4.4. Pyrolysis parameters

Results of S_2, T_{max} and HI are shown in Supplementary Data, Table S1 and on Fig. 9. For Unit C, S_2 ranges from 0.2 mg HC/g rock to 14.62 mg HC/g rock with an average of 6.86 mg HC/g rock, and HI values range from 34.3 mg HC/g TOC to 360.99 mg HC/g TOC with a mean of 208.24 mg HC/g TOC. Three high S_2 and HI values correspond to the three sharp short-term negative $\delta^{13}C_{org}$ excursions respectively. T_{max} of mudstones in Unit C ranges from 426 °C to 463 °C with an average of 440 °C.

5. Discussion

5.1. Stratigraphic correlation and the position of the OAE 1b

Zircon U-Pb dating of the tuffaceous claystone near the bottom of Unit C (1225.5 m) gave an age of 112.6 ± 1.7 Ma (Fig. 9). This age constrains the lower part of Unit C to the early Albian. A comprehensive analysis of Cretaceous strata in northeastern China based on floras, sporopollen assemblages and conchostracan faunas shows that the middle and upper Yingcheng Formation in the Songliao Basin correlates with the Shahai Formation in the Fuxin Basin (Xi et al., 2019). Zircon U-Pb ages of the Yingcheng Formation are between ~119–109 Ma (Zhang et al., 2011). These data show that the Yingcheng and Shahai formations were deposited in the late Aptian-early Albian. In addition, the middle member of the Yingcheng Formation can correlate with the Paquier level of OAE 1b, which is well constrained by single zircon U-Pb isotopic dating, palaeobotanical and palynological data (Sun et al., 2016). The Denglouku Formation in the Songliao Basin corresponds to the Fuxin Formation in the Fuxin Basin (Xi et al., 2019). *Cicatricosisporites exilis-Hymenozonotriletes mesozoicus* assemblage in the Denglouku Formation is a typical Albian flora in North China. *Kraeuselisporites majus*, *Scopusporis lautus* and *Balmeisporites holodictyus* of this assemblage are found in North America and Australia in Albian strata (Huang et al., 2011). Based on biostratigraphic studies, it can be inferred that the Fuxin Formation is of the Albian age.

Furthermore, C-isotope stratigraphic studies of the Aptian-Albian interval indicate that the globally observed breakpoint between the end of the uppermost Aptian positive $\delta^{13}C_{org}$ excursion and the onset of the pronounced negative $\delta^{13}C_{org}$ shift can

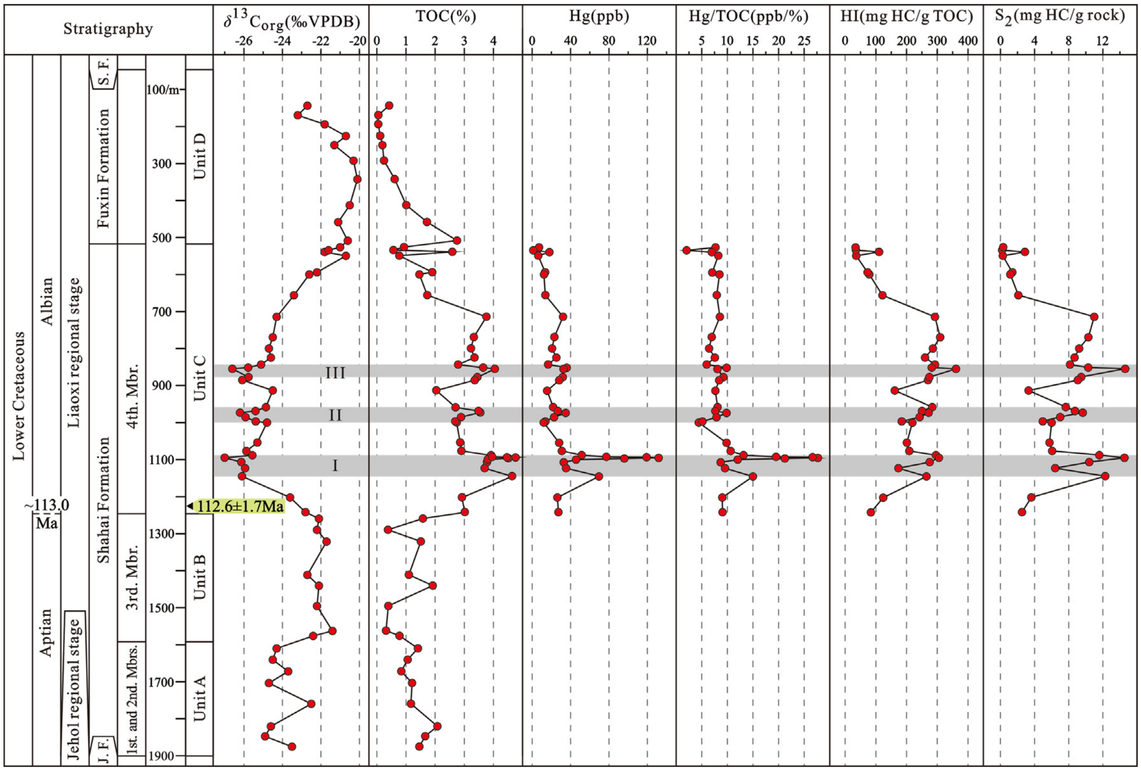

Fig. 9. Stratigraphic distribution of $\delta^{13}C_{org}$ (‰VPDB), total organic carbon (TOC, %), mercury concentration (Hg, ppb), Hg/TOC (ppb/%), hydrogen index (HI, mg HC/g TOC) and S_2 (mg HC/g rock) records for mudstones samples of borehole DY-1 from the Lower Cretaceous Shahai and Fuxin formations in the Fuxin Basin. Grey shaded intervals I, II and III represent the inferred Kilian, Paquier and Leenhardt sub-events of OAE 1b, respectively. The Aptian/Albian boundary is defined by the break point between the end of the uppermost Aptian positive $\delta^{13}C_{org}$ excursion and the onset of the pronounced negative $\delta^{13}C_{org}$ shift (Herrle et al., 2004). Zircon U-Pb dating of the tuffaceous claystone near the bottom of Unit C (1225.5 m) gave an age of 112.6 ± 1.7 Ma. Abbreviations: J. F. = Jiufotang Formation; S. F. = Sunjiawan Formation.

be used as a criterion to define the Aptian/Albian boundary in marine and terrestrial organic and inorganic carbon isotope records (Herrle et al., 2004). In the study area, the onset of pronounced negative shift of $\delta^{13}C_{org}$ values at the boundary between Unit B and Unit C (Fig. 9) is consistent with the carbon isotope record of the Aptian to Lower Albian identified by Herrle et al. (2004), which can approximately infer the position of the Aptian/Albian boundary.

5.2. Recognition of OAE 1b sub-events

5.2.1. Kilian sub-event

The Kilian sub-event is the organic-rich expression of the second sub-event of OAE 1b (Coccioni et al., 2014). Most studied successions in western Tethys show that the thickness of the Kilian sub-event varies between 0.2 m and 8 m with the TOC content up to 1%–6% (e.g., Bralower et al., 1999; Li et al., 2016). In the Poggio le Guaine section of the Umbria-Marche Basin, central Italy, this sub-event is 40 cm-thick with the TOC content up to ~1% (Coccioni et al., 2014; Sabatino et al., 2015). In the Col de Pré-Guittard section of the Vocontian Basin, this level is ~74 cm-thick with a TOC content up to 3.3% and also includes the organic matter of terrestrial origin (e.g., Herrle, 2002).

The Kilian sub-event also exhibits a distinct negative carbon isotope excursion in western Tethys and North Atlantic Ocean, where the black mudstone horizon defined by a distinct negative carbon isotope excursion, considered in the past as the Paquier sub-event equivalent (e.g., Herrle, 2002; Herrle et al., 2004; Friedrich et al., 2005), has to be regarded as a Kilian sub-event equivalent as also pointed out by Trabucho Alexandre et al. (2011) and Coccioni et al. (2014). At DSDP Site 545, Mazagan Plateau, eastern North Atlantic, the Kilian sub-event is 60 to 80 cm-thick with a TOC content up to ~5% and shows a distinct negative carbon isotope excursion from ~2‰ prior to the organic-rich interval to an average value of 0.75‰ during the sub-event and a gradual return to carbon isotopic values of ~1.2‰ at its termination (e.g., Herrle, 2002; Herrle et al., 2004; Friedrich et al., 2005; Trabucho Alexandre et al., 2011). In the Andean Basin, northern Peru, the Kilian sub-event is characterized by a large negative $\delta^{13}C_{org}$ excursion with an abrupt negative shift reaching −26.3‰ (Navarro-Ramirez et al., 2015). In the terrestrial records of OAE 1b from southeastern China, the Kilian sub-event shows a negative excursion with an average $\delta^{13}C_{org}$ value of −26.1‰, occurs at the 44.4–44.7 m depth in the Shipu section and an average $\delta^{13}C_{org}$ value of −27.0‰ in the Chong'an section (Hu et al., 2014).

In the Fuxin Basin, event I, a negative $\delta^{13}C_{org}$ excursion can be observed at the interval of 1146–1088.3 m with a decrease from −26.1‰ to −27‰ and a gradual return to $\delta^{13}C_{org}$ value of −25.6‰ at its termination. The peak value of negative $\delta^{13}C_{org}$ excursion corresponds to a high TOC value up to 4.76% during the event I. Moreover, a relatively small negative $\delta^{13}C_{org}$ excursion above the negative excursion of the event I can be seen at the interval of 1088.3–1000 m. Comparing to the typical change trend of carbon isotope from the Vocontian basin (Fig. 10), there are one or two negative shifts of carbon isotope between the Kilian and Paquier sub-events (Herrle et al., 2004). The carbon isotopic records in the event I is the first distinct negative $\delta^{13}C_{org}$ excursion above the top of the positive $\delta^{13}C_{org}$ excursion, which is consistent with the characteristics of the Kilian sub-event, a short negative excursion above the positive excursion in the carbon isotope record of the Jacob sub-event (Herrle et al., 2003; Herrle et al., 2004). In addition, the age of the event I is approximately younger

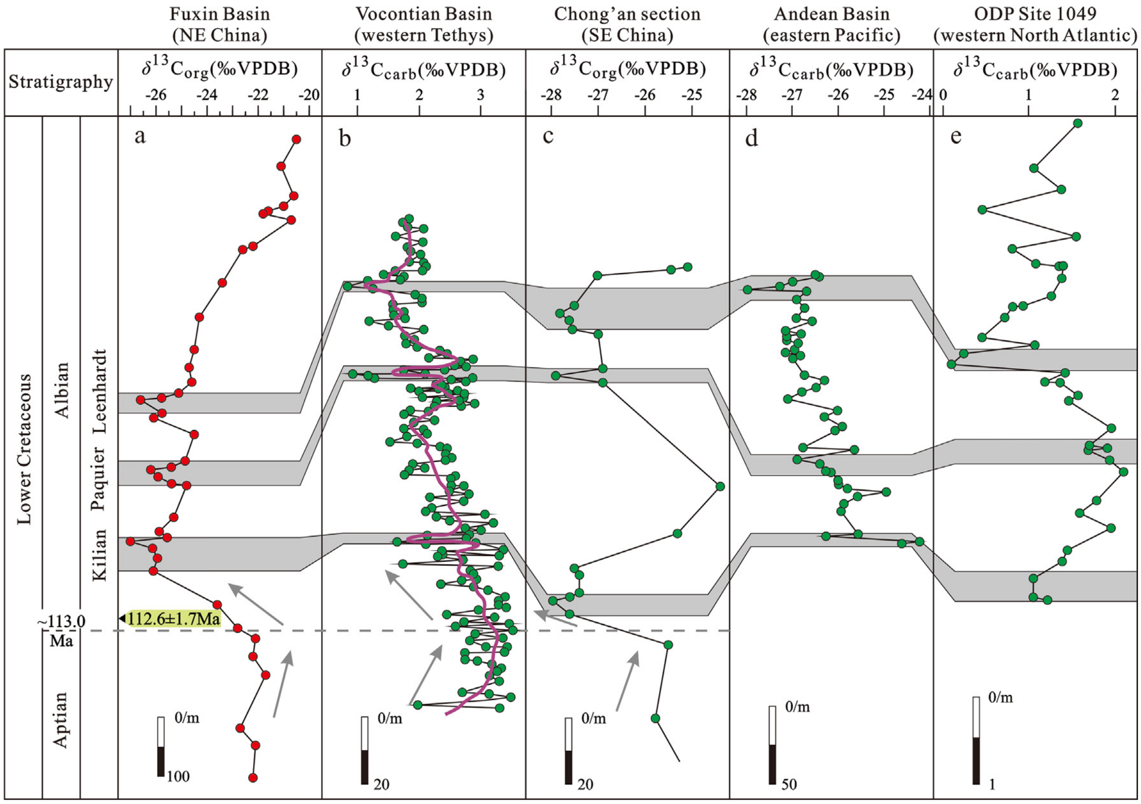

Fig. 10. Correlation of the early Albian OAE 1b carbon isotope changes from published studies on the western Tethys, eastern Pacific, western North Atlantic and China. (a) Carbon isotope curve of lacustrine mudstones from the Fuxin Basin, NE China (this work). (b) Carbon isotope curve of carbonates from the Vocontian basin, SE France (western Tethys) (Herrle et al., 2004). (c) Carbon isotope curve of terrestrial sediments from the Chong'an section, SE China (Hu et al., 2014). (d) Carbon isotope curve of carbonates from the Andean basin, northern Peru (eastern Pacific) (Navarro-Ramirez et al., 2015). (e) Carbon isotope curve of carbonates from ODP site 1049 off northern Florida, Blake Nose escarpment (western North Atlantic) (Huber et al., 2011). Time-equivalent sub-events (Kilian, Paquier and Leenhardt sub-events) of OAE 1b are correlated with grey shading.

than 112.6 ± 1.7 Ma according to the zircon U-Pb dating analysis (Fig. 9). According to the above observations, we interpret that the negative $\delta^{13}C_{org}$ excursion of event I could be the counterpart of the Kilian sub-event.

5.2.2. Paquier sub-event

The Paquier sub-event is the organic-rich expression of the third sub-event of OAE 1b, which is well documented in western Tethys, western North Atlantic and Mexico (e.g., Erbacher et al., 2001; Tsikos et al., 2004; Trabucho Alexandre et al., 2011; Coccioni et al., 2014). The representative study in the Vocontian Basin shows that the Paquier sub-event is 1.63 m-thick with the average TOC value generally above 3% and maximum values of 8% and with terrestrial and marine organic matter in variable proportions (e.g., Herrle, 2002). In the Poggio le Guaine section of the Umbria-Marche Basin, this sub-event is 25 cm-thick with TOC value up to 9.8% (Coccioni et al., 2014; Sabatino et al., 2015).

The Paquier sub-event of OAE 1b is defined by a negative excursion in both marine carbonate (1.5‰–2‰) and organic matter (~3‰) carbon isotope records (e.g., Bralower et al., 1999; Erbacher et al., 2001; Herrle et al., 2004; Tsikos et al., 2004). In the Andean Basin, the Paquier sub-event starts with an abrupt negative $\delta^{13}C_{carb}$ shift reaching value as low as 0.1‰, while $\delta^{13}C_{org}$ value exhibits a gradual negative shift reaching −27‰ (Navarro-Ramirez et al., 2015). The terrestrial records of OAE 1b from southeastern China show that the Paquier sub-event, a strongest negative excursion with a $\delta^{13}C_{org}$ peak value of −27.8‰, is an approximately 30 cm-thick in the Shipu section and an average $\delta^{13}C_{org}$ value of −27.9‰ in the Chong'an section (Hu et al., 2014).

In the study area, the negative $\delta^{13}C_{org}$ excursion of event II occurs at the 1000–958.5 m depth, with a decrease from −24.8‰ to −26.2‰ and a subsequent gradual return to an isotopic value of 24.9‰ at end of the interval. The $\delta^{13}C_{org}$ values exhibit a gradual negative shift reaching −26.2‰ with 1.4‰ change extent, which well matches the magnitude of $\delta^{13}C_{org}$ change ~1.5‰ of terrestrial records, such as fossil wood from Japan (Ando and Kakegawa, 2007), palustrine carbonate nodules from USA (Ludvigson et al., 2010), and terrestrial organic matter from southeastern China (Hu et al., 2014). In terms of the magnitude of carbon isotope greater than 1‰ (Navarro-Ramirez et al., 2015), the event II in the Fuxin Basin could be comparable with the Paquier sub-event of OAE 1b. High resolution carbon isotope records from the Vocontian Basin show that the Paquier sub-event is above the Kilian sub-event and its carbon isotope exhibits a short and maximum negative excursion after a short recovery above the Kilian sub-event (Fig. 10; Herrle et al., 2004). This similar pattern of negative $\delta^{13}C_{org}$ shift was observed in event II, which suggests that the Paquier sub-event equivalence is probably recorded in Fuxin Basin.

5.2.3. Leenhardt sub-event

The Leenhardt level was mainly documented in western Tethys (Coccioni et al., 2014; Li et al., 2016). In the Col de Palluel section of the Vocontian Basin, this sub-event is ~92 cm-thick with a TOC content up to 3% and contains organic matter of marine origin (e.g., Herrle, 2002). At the Poggio le Guaine section of the Umbria-Marche Basin, it is 29 cm-thick with a TOC content of 0.95% (Coccioni et al., 2014) to 1.1% (Sabatino et al., 2015).

The Leenhardt sub-event is also represented by negative excursion of carbon isotope records in different study areas (e.g., Huber et al., 2011; Coccioni et al., 2014; Li et al., 2016). In western Tethys, the Leenhardt sub-event is defined by a negative $\delta^{13}C_{carb}$ excursion of ~1‰ at the Poggio le Guaine section of the Umbria-Marche Basin (Coccioni et al., 2014). In the Andean Basin, the Paquier sub-event shows a sharp $\delta^{13}C_{carb}$ decrease reaching −0.1‰ and a negative $\delta^{13}C_{org}$ excursion decrease down to values as low as −28‰ (Navarro-Ramirez et al., 2015). In southeastern China, the terrestrial records of Leenhardt sub-event show a relatively weak negative $\delta^{13}C_{org}$ excursion with an average $\delta^{13}C_{org}$ value of −27.6‰ in the Chong'an section (Hu et al., 2014).

In the Fuxin Basin, event III, a negative $\delta^{13}C_{org}$ excursion occurred at the interval of 877.7–843.3 m depth can be observed. The $\delta^{13}C_{org}$ values decrease from −25.7‰ to −26.6‰, then a positive $\delta^{13}C_{org}$ excursion takes place with the $\delta^{13}C_{org}$ values up to −25.1‰. The magnitude of the negative $\delta^{13}C_{org}$ excursion by 1.5‰ during the event III is similar to those of platform carbonates in the Andean Basin (Navarro-Ramirez et al., 2015) and the ODP site 1049 off northern Florida, Blake Nose escarpment, western North Atlantic (Huber et al., 2011), but higher than those of hemipelagic and platform carbonates in Tethys, such as Umbria-Marche Basin (Coccioni et al., 2014) and Bangbu section, southern Tibet, China (Li et al., 2016). The negative excursion with a $\delta^{13}C_{org}$ peak value reaching −26.6‰ is even comparable to that of terrestrial records from southeastern China (Fig. 10; Hu et al., 2014) and that of organic matter in the Andean Basin (Fig. 10; Navarro-Ramirez et al., 2015). Therefore, we interpret that the negative excursion of event III, observed in $\delta^{13}C_{org}$ records from Fuxin Basin, could be the Leenhardt sub-event equivalence.

The OAE 1b spans from the late Aptian to early Albian and is characterized by a significant negative shift of carbon isotopes and enhanced carbon burial (Bralower et al., 1999; Leckie et al., 2002; Tsikos et al., 2004; Herrle et al., 2004). Three sub-events (Kilian, Paquier and Leenhardt sub-events) of OAE 1b are characterized by distinct negative carbon isotope excursions in the early Albian (Li et al., 2016; Sabatino et al., 2015). In the study area, three sharp, short-term negative $\delta^{13}C_{org}$ excursion events I, II and III all correspond with relatively high TOC values, which is well correlated with three sub-events (Kilian, Paquier and Leenhardt sub-events) of the early Albian OAE 1b. Furthermore, carbon isotopic results of this study compare well with four representative research cases including western Tethys, eastern Pacific, western North Atlantic and southeastern China. As shown in Fig. 10, the three distinct negative $\delta^{13}C_{org}$ excursion events I, II and III in Unit C during the early Albian are well correlated to the three sub-events (Kilian, Paquier and Leenhardt sub-events) of OAE 1b, suggesting that the global OAE 1b has not only a marine but also a terrestrial record.

5.3. Changes in atmospheric CO_2 concentrations

Recent laboratory work has suggested that pCO_2 may affect the net isotopic discrimination ($\Delta\delta^{13}C_p$) between the carbon isotope composition of C_3 plant tissue ($\delta^{13}C_{org}$) and that of atmospheric CO_2 ($\delta^{13}C_{CO2}$), which results in a hyperbolic relationship between $\Delta\delta^{13}C_p$ and pCO_2 (e.g., Schubert and Jahren, 2012; Cui and Schubert, 2017; Barral et al., 2017a; Lomax et al., 2019). pCO_2 values were estimated in this study using the equation relating pCO_2 to $\delta^{13}C_{org}$ described by Schubert and Jahren (2012) as:

$$\Delta\delta^{13}C_p = [A \times B \times (pCO_2 + C)]/[A + B \times (pCO_2 + C)] \quad (1)$$

where $\Delta\delta^{13}C_p$ values were estimated from $^{13}C_{org}$ value incorporated into C_3 plant material and concomitant $\delta^{13}C_{CO2}$ value by using the equation proposed by Farquhar et al. (1989): $\Delta\delta^{13}C_p = (\delta^{13}C_{CO2} - \delta^{13}C_{org})/(1 + \delta^{13}C_{org}/1000)$. While the A value varies between 26 and 30, Schubert and Jahren (2012) found the best-fitting curve corresponds with A = 28.26, and this value has been used in many studies (e.g., Schubert and Jahren, 2013; Cui and Schubert, 2017). B and C have been determined by iterative curve fitting for B = 0.21 and C = 25 (Schubert and Jahren, 2012). In this study, the $\delta^{13}C_{CO2}$ value of atmospheric CO_2 is based on $\delta^{13}C_{CO2}$ estimates of bulk marine carbonates for the Cretaceous time period (Barral et al., 2017b). The $\delta^{13}C_{org}$ values of units A, B, C and D vary from −20.1‰ to −27‰, which is in the range of C_3 plants with $\delta^{13}C_{org}$ values between −20‰ and −32‰ (Leavitt, 2009). Therefore, we used the relationship between pCO_2 and $\delta^{13}C_{org}$ to estimate pCO_2 during the Early Cretaceous.

The Cretaceous represents a typical greenhouse climate period in Earth's history (Wang, 2006). As one of the primary greenhouse gases, the reconstruction of atmospheric CO_2 is crucial for understanding the Cretaceous greenhouse, which has been recorded in previous studies about the atmospheric CO_2 levels throughout the Cretaceous (e.g., Hong and Lee, 2012; Barral et al., 2017a). Barral et al. (2017a) reconstructed a long-term evolution of pCO_2 throughout the Cretaceous from the $\delta^{13}C_{org}$ of the fossil conifer *Frenelopsis* and showed that pCO_2 was in the range of 150–650 ppm during the Barremian–Santonian interval. In the study area, the variations in pCO_2 (139.2–528.6 ppm, average 279.7 ppm) during units A, B, C and D (Fig. 11) are similar to the atmospheric CO_2 levels estimated from the fossil conifer *Frenelopsis* (Barral et al., 2017a), and our pCO_2 record shows a trend of increasing pCO_2 during the early Albian, which is even comparable to a small increase based on stomata data in the same time interval (Haworth et al., 2005; Hong and Lee, 2012). However, our pCO_2 results are lower than the atmospheric CO_2 estimates based on the carbon isotope and stomatal data of Cheirolepidiaceae from the Early Cretaceous Jiuquan Basin, northwestern China (Du et al., 2016).

OAEs record profound changes in the climatic condition and represent major disturbances in the global carbon cycle (Leckie et al., 2002; Jenkyns, 2010). The prevailing model for the major forcing function behind OAEs was an abrupt temperature rise, induced by the rapid influx of CO_2 into the atmosphere from volcanogenic and/or methanogenic sources (Jenkyns, 2010; Robinson et al., 2017). Sun et al. (2016) estimated atmospheric CO_2 concentrations based on Gingko leaves during the latest Aptian–earliest Albian OAE 1b, which were slightly higher than data between the early Aptian OAE 1a and the middle Aptian Fallot OAEs. In the study area, pCO_2 in Unit A during the early part of the late Aptian (212–332.5 ppm, average 287.2 ppm) and Unit B during the latest Aptian (174.6–219.7 ppm, average 198 ppm) were relatively low with high fluctuations. In Unit C during the early Albian, pCO_2 concentrations (154.6–528.6 ppm, average 331.8 ppm) increased noticeably. In Unit D during the middle and late Albian, a relative decrease in the pCO_2 (139.2–240.5 ppm, average 172.4 ppm) occurred. The resulting estimates of atmospheric CO_2 concentrations indicate that a trend of increasing pCO_2 during the early Albian, and there are three short-term increases of pCO_2 corresponding to the Kilian, Paquier and Leenhardt sub-events of the OAE 1b.

5.4. Palaeoclimate and continental weathering changes

Previous studies considered that there is geochemical evidence for increased continental weathering, accompanied by an increase in temperature and humidity during OAEs (Leckie et al., 2002; Herrle et al., 2003; Friedrich et al., 2005; Jenkyns, 2010). According to the analysis of calcareous nannofossils, palynomorphs, benthic foraminifera and oxygen isotopes, the formation of Kilian and Paquier sub-events of OAE 1b occurred under increasingly warm and humid conditions (Herrle et al., 2003). Many previous studies

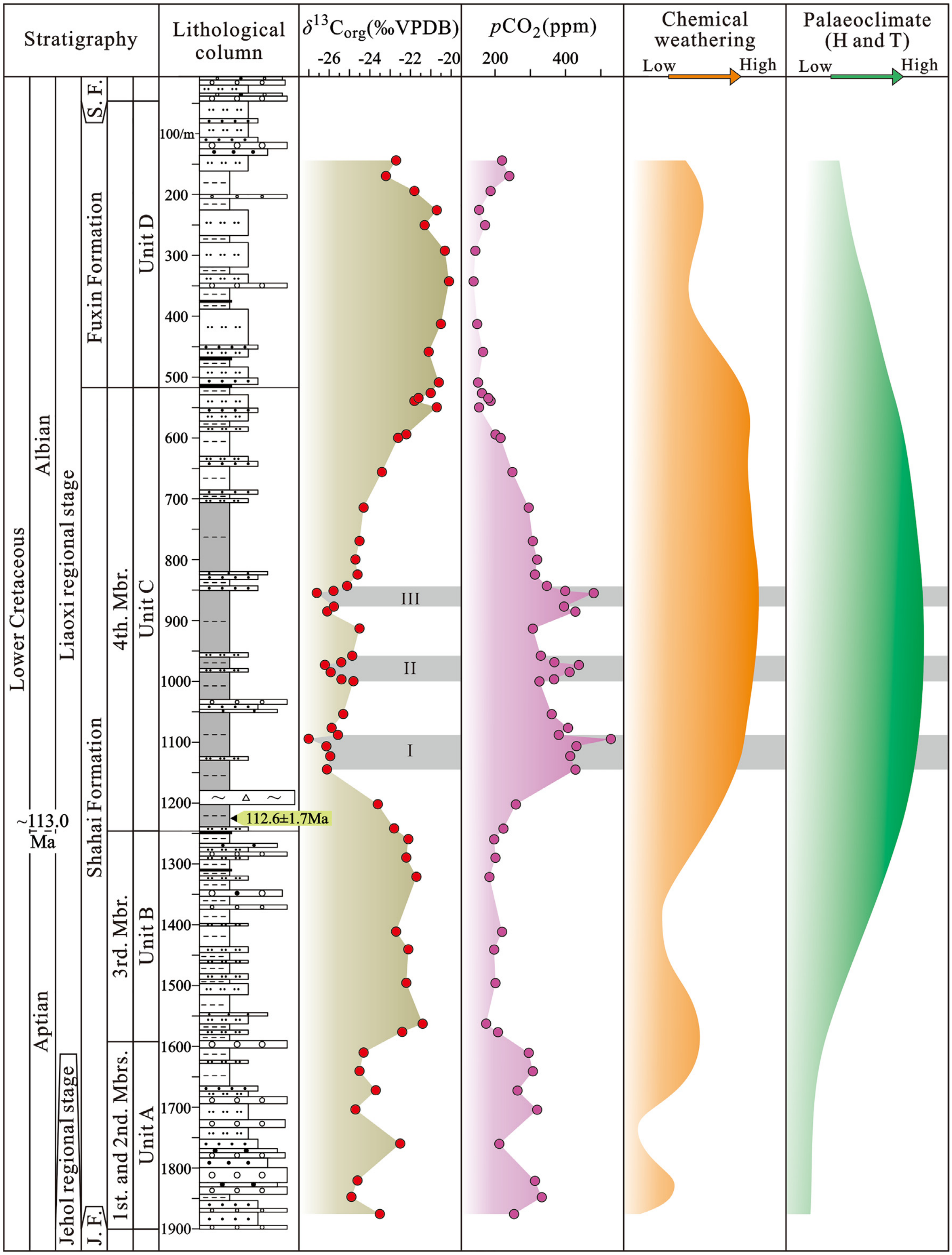

Fig. 11. Lithological column of units A, B, C and D in the Fuxin Basin and stratigraphic records of $\delta^{13}C_{org}$ (‰VPDB), pCO$_2$ (ppm), chemical weathering (modified after Xu et al., 2020a) and palaeoclimate (humidity and temperature) inferred from palynoflora (modified after Wan et al., 2017). H and T represent humidity and temperature, respectively. Grey shaded intervals I, II and III represent the Kilian, Paquier and Leenhardt sub-events of OAE 1b, respectively. Thick-bedded black mudstones are highlighted in the lithological column. Key to lithologic symbols is shown in Fig. 3. Abbreviations: J. F. = Jiufotang Formation; S. F. = Sunjiawan Formation.

suggested that increasing Sr isotope ratios ($^{87}Sr/^{86}Sr$) have been linked to intensified continental weathering (e.g., Bralower et al., 1997; Jones and Jenkyns, 2001). Sr isotope values over OAE 1b interval indicate a relative increase in radiogenic strontium to the oceans, which could be interpreted as reflecting accelerated continental weathering in response to elevated global temperature (Bralower et al., 1997). In the l'Arboudeysse section of the Vocontian Basin, Paquier sub-event of OAE 1b is characterized by three significant increases in kaolinite contents, Weathering Index (WI) and Chemical Index of Alteration (CIA), which suggest the development of intense chemical weathering under more humid conditions during this interval (Benamara et al., 2020).

Chemical weathering indices are sensitive to climate, with higher values favored by relatively warm and humid conditions and lower values associated with cold and dry climates (Nesbitt and Young, 1982). In addition to above mentioned CIA, the Mafic Index of Alteration for Oxidative weathering environments ($MIA_{(O)}$; Babechuk et al., 2014) suggesting the ratio of stable residual elements relative to labile elements, and Weathering Index of Parker (WIP; Parker, 1970) showing the bond strengths of the most mobile alkali and alkaline elements with oxygen have been considered to analyze the chemical weathering degree in the Fuxin Basin during units A, B, C and D (Xu et al., 2020a). In the study area, in Unit A, CIA (54.7–73.1, average 63.4) and $MIA_{(O)}$ (42.6–55.7, average 50) values were relatively low and showed characteristic high fluctuations, while WIP values (34–65.5, average 53.8) were relatively high and experienced high amplitude fluctuations (Xu et al., 2020a). These results suggest that the degree of chemical weathering was relatively low and show evidence for high amplitude fluctuations under relatively low temperatures and dry palaeoclimate conditions. The weakening trend of chemical weathering in Unit A could indicate a response to relatively global climate cooling during the late Aptian (Weissert and Lini, 1991; McAnena et al., 2013). During Unit B, CIA (62.6–71.8, average 67.9) and $MIA_{(O)}$ (54.1–63.7, average 58.9) values increased noticeably but maintained high amplitude fluctuations, while the WIP values (33.2–50, average 41.8) decreased but still fluctuated unsteadily (Xu et al., 2020a). This unit was a transitional period that indicates fluctuating degrees of chemical weathering and palaeoclimate. In Unit C, CIA (62.4–72.6, average 67.1), $MIA_{(O)}$ (53.8–63.1, average 58.3) and WIP (38.6–54.9, average 46.7) values tended to be relatively stable after a transition period, which shows evidence for enhanced chemical weathering and warm, humid palaeoclimates (Xu et al., 2020a). During Unit D, relative decreases in CIA (60.9–74.7, average 68.6) and $MIA_{(O)}$ (49.8–63.6, average 57.5) values are evidenced, but an increase in WIP (42.5–58.8, average 47.5) shows that the chemical weathering intensity had a downward trend, reflecting a gradual deterioration of warm and humid palaeoclimatic conditions (Xu et al., 2020a). In addition, based on palaeoclimate evolution inferred from palynoflora in northeastern China (Wan et al., 2017), humidity and temperature increased and then decreased through the late Aptian-early Albian interval (Fig. 11), which is consistent with the trends of chemical weathering. Although the data of chemical weathering indices can't correspond to the data of $\delta^{13}C_{org}$ and TOC, these chemical weathering indices reflect the same change trends of chemical weathering, which could indicate accelerated continental weathering under warmer and more humid conditions during OAE 1b interval.

$\delta^{13}C_{org}$ values of plant tissues are influenced by environmental factors such as pCO_2, temperature, mean annual precipitation (MAP) and light (Nguyen Tu et al., 2004; Kohn, 2010). A broad compilation of modern carbon isotope compositions in all C_3 plant types shows a monotonic increase in $\delta^{13}C_{org}$ with decreasing MAP, among these, high $\delta^{13}C_{org}$ values (above −25.5‰) are essentially restricted to environments with MAP less than 500 mm/yr (Kohn, 2010). In the study area, $\delta^{13}C_{org}$ values of units A (−24.9‰ to −22.5‰), B (−22.7‰ to −21.4‰) and D (−23.2‰ to −20.1‰) examined in the Fuxin Basin are mostly higher than −25.5‰ (Fig. 11), indicating that MAP during deposition of three units was lower than 500 mm/yr and thus relatively dry. The $\delta^{13}C_{org}$ values of Unit C vary from −27‰ to −20.7‰, and the $\delta^{13}C_{org}$ values of 66.7% samples during the three sub-events of OAE 1b are less than −25.5‰, which indicates that the MAP during OAE 1b was relatively increased, reflecting a gradual increase of humid climate.

5.5. Source of organic matter

Previous studies of organic matter characteristics during the OAE 1b interval show that the terrestrial nutrient element input could have played an important role in stimulating the primary productivity linked to the Kilian, Paquier and Leenhardt sub-events of OAE 1b (Erbacher et al., 1996; Trabucho Alexandre et al., 2011; Coccioni et al., 2014). To quantify terrestrial input, the terrigenous/marine ratio (TMR) of palynomorphs was calculated (e.g., Pross, 2001). The rapid TMR increase during the formation of the Kilian and Paquier sub-events of OAE 1b indicates enhanced terrestrial input into the Vocontian Basin (Herrle et al., 2003). Similarly, higher detrital index values indicate a general increase in detrital input from the continent to the ocean during the Paquier sub-event of OAE 1b, which can be linked to an acceleration of the hydrological cycle and increased continental weathering (Benamara et al., 2020). In addition, the relationship between the various types of kerogens and specific geological settings suggests that type II kerogen can be associated with planktonic organic matter in open marine and fresh water lacustrine environments, and that type III kerogen is sourced from terrestrial plants (Vandenbroucke and Largeau, 2007). The hydrogen and oxygen indices obtained from pyrolysis analyses show that organic-rich sediments of the Kilian and Paquier sub-events of OAE 1b consist of type II and III kerogens, which indicate that the organic matter is composed of a mixture of marine and terrestrial sources (Trabucho Alexandre et al., 2011). The terrestrial records of OAE 1b from southeastern China also suggest that a mixture of terrestrial plants and algae might be associated with the formation of OAE 1b (Hu et al., 2014).

In the study area, the T_{max} values range between 426 °C and 463 °C with a mean value of 440 °C in Unit C (Table S1). The maturity determined by T_{max}, suggests that most of the samples lie within the mature zone of hydrocarbon generation (430–465 °C; Espitalié et al., 1985). The relationship between the pyrolysis parameters HI and T_{max} shows that organic matters of the three sub-events of OAE 1b consist of type II and III kerogens, which indicates that the organic matters are composed of mixed sources of terrestrial plants and lacustrine plankton (Fig. 12a). Data from Unit C with TOC less than 5% are plotted on an S_2 vs. TOC diagram (Fig. 12b), which also suggests a predominance of a mixture of type II and III kerogens during the three sub-events of OAE 1b. Mudstones that contain type II kerogen reflect an increase in organic productivity of lacustrine plankton, which can be linked to enhanced nutrients flushed into the Fuxin lacustrine basin during the early Albian OAE 1b. In addition, abundant mudstones containing type III kerogen are related to intensified transport rates of terrestrial plants into the lake, caused by an accelerated hydrological cycle and increased continental weathering. Pyrolysis analyses support a terrestrial contribution to the organic-rich sediments of the Kilian, Paquier and Leenhardt sub-events of OAE 1b.

5.6. Possible driving mechanisms for OAE 1b

Fuxin Basin is a continental faulted basin, and the development of sedimentary environments in the interior of the basin was controlled by fault activity on the basin margins (Liu et al., 1992; Li, 1988; Zhu et al., 2007). In the early history of the Shahai Formation, fault activity along basin margins intensified, and the eastern and western margins of the basin were uplifted and eroded (Liu et al., 1992). The first and second members of the Shahai Formation are mainly composed of conglomerates and coarse-grained sandstones. An alluvial fan depositional system is inferred for the interior margins of the basin, and alluvial plains developed in front of and between the alluvial fans. With the outward expansion of the basin, the margins of the basin continuously supplied detrital

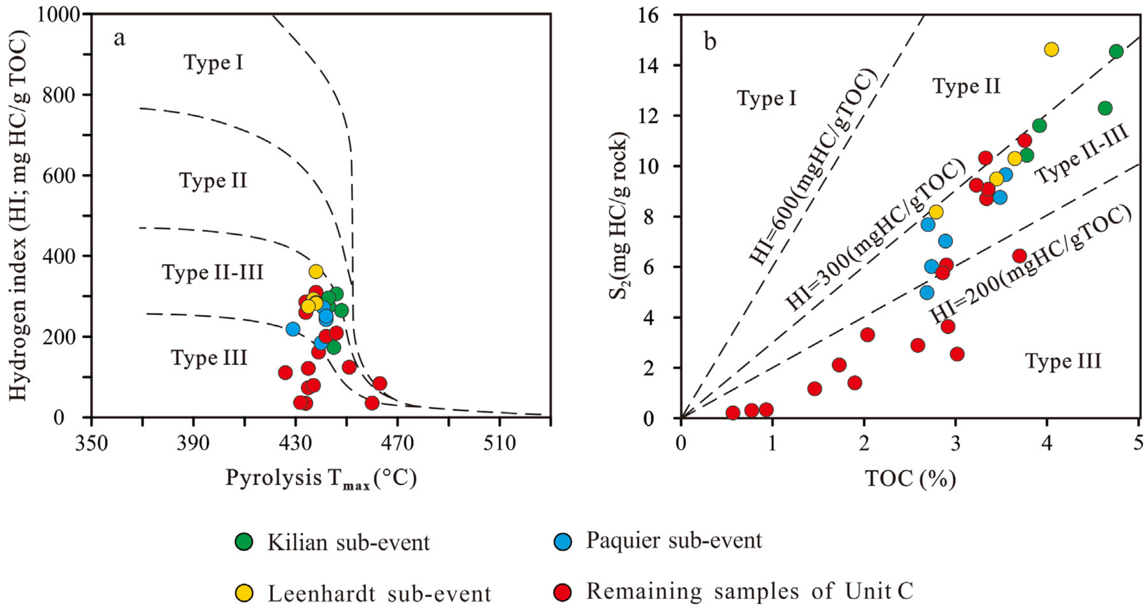

Fig. 12. (a) Cross plot of hydrogen index (HI) and pyrolysis T_{max} of mudstone samples from the Kilian, Paquier and Leenhardt sub-events of OAE 1b, on a base proposed by Mukhopadhyay et al. (1995). (b) Binary plot of TOC vs. S_2 for mudstone samples from the Kilian, Paquier and Leenhardt sub-events of OAE 1b. Base is from Langford and Blanc-Valleron (1990).

material to the interior of the basin (Zhu et al., 2007). During the middle period of the Shahai Formation, fault activity along basin margins continued to increase (Liu et al., 1992). The third member of the Shahai Formation consists predominantly of fan delta and lacustrine depositional systems characterized by coal-bearing strata. During the late period of the Shahai Formation, under conditions increased fault activity along the basin margins, the Fuxin Basin expanded to its greatest aerial extent and deepest water conditions (Zhu et al., 2007). The thick-bedded, black mudstones of the fourth member of the Shahai Formation (Fig. 6) developed under these conditions. A large number freshwater fauna comprising gastropods and bivalves were identified in lacustrine sedimentary facies (Figs. 3, 4e, 4f, 4g and 8a). In the Fuxin Formation, the basin no longer continued to expand, the rate of basement subsidence began to slow, and the lake water gradually shallowed (Li, 1988; Zhu et al., 2007). Under these conditions, fluvial and swamp conditions prevailed as represented by sandstones and mudstones with coal seams. Based on the analysis of Fuxin lacustrine basin evolution, the genesis of thick, organic-rich black mudstones during the fourth member of the Shahai Formation are further discussed below.

LIP volcanism has been considered as an important trigger of environmental perturbations, including climate, sea level, oceanic anoxia and biological extinctions (Leckie et al., 2002; Shen et al., 2019). Many studies suggest a link between the OAE 1b and the emplacement of the Kerguelen LIP in the early Albian (e.g., Bralower et al., 1999; Leckie et al., 2002; McAnena et al., 2013; Sabatino et al., 2018). Recent studies have suggested that Hg enrichments have become an efficient tool for tracing volcanism and LIP activity in the sedimentary record (e.g., Grasby et al., 2013, 2019; Shen et al., 2019; Dal Corso et al., 2020). In the study area, we observe a good correspondence between the Kilian sub-event and the anomalies of Hg and Hg/TOC (Fig. 9), which could indicate that there is a record of volcanic activity during the Kilian sub-event interval. This record is in agreement with previous studies that connected the deposition of black mudstones during the Kilian sub-event to the volcanic activity of the Kerguelen LIP (e.g., Trabucho Alexandre et al. 2011; Coccioni et al., 2014; Sabatino et al., 2018). The record of Hg and Hg/TOC anomalies may represent an enhanced pulse in volcanic activity of the Kerguelen LIP. Three distinct, short-term negative $\delta^{13}C_{org}$ excursions have been documented in the Fuxin Basin during the Kilian, Paquier and Leenhardt sub-events of the early Albian OAE 1b, which coincides with the intervals of elevated pCO_2. Under these conditions of increasing pCO_2, ^{12}C-enriched CO_2 will have been preferentially fixed through photosynthesis of plants (Park and Epstein, 1960) and transferred to terrestrial and marine strata, leading to contemporaneous records of negative $\delta^{13}C_{org}$ excursions in the Fuxin lacustrine basin. According to the above mentioned record of volcanic activity, we infer that a possible source of the increasing trend of ^{12}C-enriched CO_2 during the Kilian sub-event is volcanism from the Kerguelen LIP. However, the Hg signal displays no significant spike in the Paquier and Leenhardt sub-events, which does not provide evidence for the presence of important volcanic activity. The absence of Hg and Hg/TOC anomalies in the Paquier and Leenhardt sub-events may be caused by gradual decreasing volcanic pulses of the Kerguelen LIP. This implies that the increasing pCO_2 trend during the Paquier and Leenhardt sub-events might be related to other sources, such as methane hydrate release (Hesselbo et al., 2000) and thermogenic methane release (McElwain et al., 2005). The negative $\delta^{13}C_{org}$ excursion observed in the Fuxin Basin during the Paquier and Leenhardt sub-events may be attributed to the contribution of ^{13}C-depleted methane release, and the subsequent oxidation to CO_2.

The observation of increases in pCO_2, temperature, humidity, continental weathering and nutrients and organic matter inputs during OAE 1b black mudstone formation is in agreement with previous studies that connected the deposition of black mudstones to an accelerated hydrological cycle (e.g., Leckie et al., 2002; Herrle et al., 2003; Jenkyns, 2010). In the study area, pCO_2 recovered from $\delta^{13}C_{org}$ of C_3 plants shows an increasing trend during the early Albian OAE 1b, among them, the elevated pCO_2 during the Kilian sub-event may have been linked to the volcanic activity of the Kerguelen LIP. The comprehensive analysis of MAP, humidity and temperature characteristics inferred from chemical weathering indices and palynoflora shows that the temperature and humidity increased during the OAE 1b. In addition, the degree of chemical weathering calculated by the chemical weathering indices (CIA, WIP and $MIA_{(O)}$) had an upward trend during OAE 1b interval (Xu et al., 2020a). The mixed sources of terrestrial plants and lacustrine plankton linked to the Kilian, Paquier and Leenhardt sub-events, the transported tree trunk fossils (Fig. 8c) and the terrestrial plant fragments in organic-rich lamina (Fig. 8e) identified in the profundal lacustrine depositional system of Unit C indicate that terrestrial plants flushed into lakes and nutrients transported from continents into lakes might increase the growth of lacustrine plankton. Enhanced CO_2 concentration in the atmosphere is considered to be the main cause of global greenhouse (Larson and Erba, 1999; Yevenes et al., 2019). The increase of pCO_2 in the atmosphere aggravates the greenhouse effect during the early Albian, which might have triggered the relatively warm and humid palaeoclimatic conditions, and consequently intensified chemical weathering and transport rates of nutrients and organic matter from continents into lakes and oceans where nutrients might increase productivity in surface waters. Ultimately, nutrients and organic matter were flushed into lakes and contemporaneous oceans, where decaying organic matter in surface waters, including terrestrial plants and lacustrine plankton, consumed oxygen during downward passage through the water column, which in turn led to anoxia in lakes (Fig. 13). Many organisms gradually died and organic matter was buried and preserved with an expansion of the oxygen-minimum zone, resulting in the formation of thick, organic-rich black mudstones. In such a context, a large number of fossil fragments of gastropods and bivalves (Figs. 3, 4e, 4f, 4g and 8a) and three, thick intervals of organic-rich mudstones (Fig. 6) developed in lacustrine settings during Unit C. The relatively high TOC values documented in the Fuxin Basin during the Kilian, Paquier and Leenhardt sub-events of OAE 1b, indicates that increased burial of organic matter occurred in the context of elevated pCO_2 and enhanced continental weathering under warmer and more humid conditions. Meanwhile, it can be inferred that the massive death of these organisms and the three prominent mudstones with high TOC contents in Unit C during the early Albian might have been caused by the prevailing anoxic conditions in association with the expansion of oxygen-minimum zone.

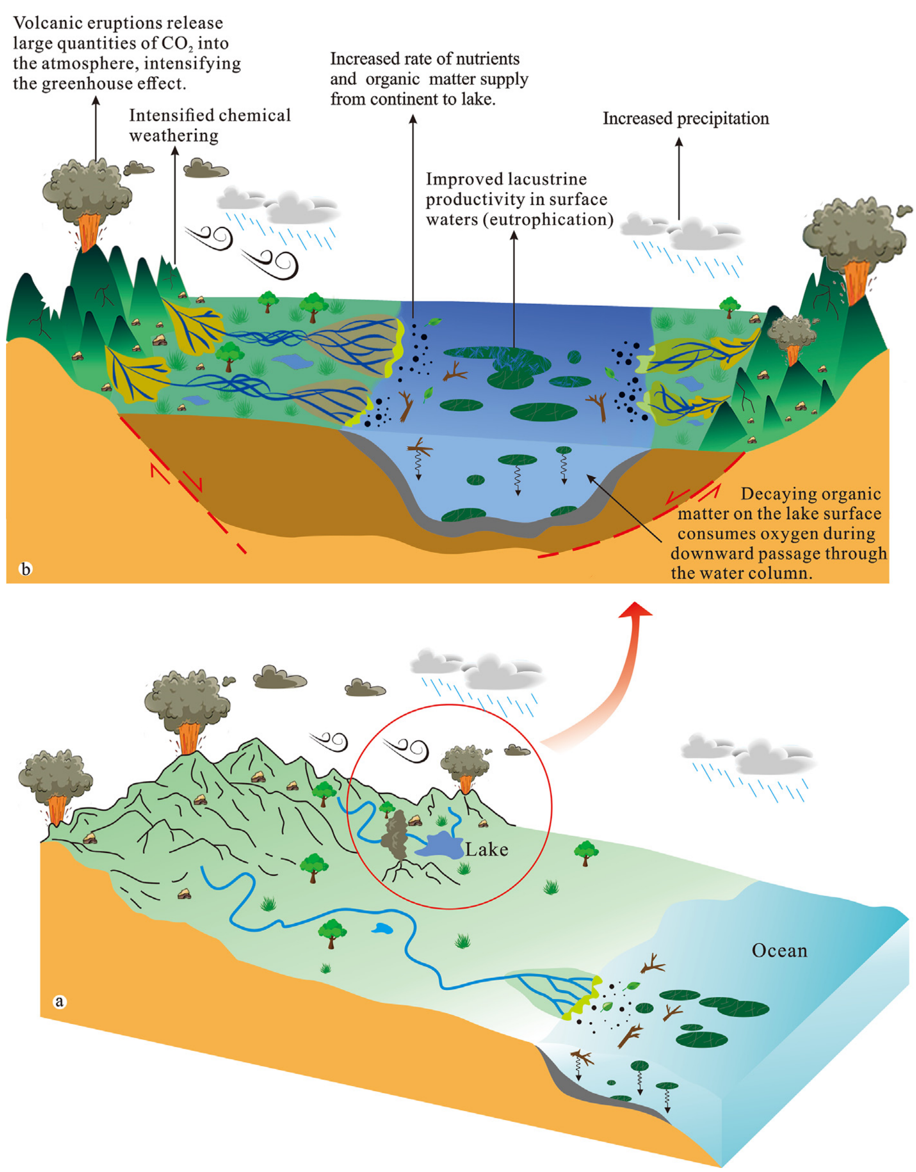

Fig. 13. (a) Schematic model for anoxia in the lake and the ocean. (b) Model to illustrate a series of processes leading to anoxia in a Fuxin lacustrine basin during the early Albian. A CO_2-forced greenhouse effect led to a warm and humid palaeoclimate that intensified continental chemical weathering and increased the transport rate of nutrients and organic matter from the continent into lakes thereby contributing to eutrophication and anoxia in lacustrine and in contemporaneous oceanic systems.

6. Conclusions

The purpose of this study is to attempt to identify terrestrial records of the early Albian OAE 1b in the Fuxin lacustrine basin and to further infer its possible driving mechanisms. The main conclusions based on this study are:

(1) Three distinct short-term negative excursions of $\delta^{13}C_{org}$ during the early Albian in the Fuxin Basin all correspond to relatively high TOC values, termed events I, II and III. We infer events I, II and III to be the counterparts of the Kilian, Paquier and Leenhardt sub-events of OAE 1b, because three negative $\delta^{13}C_{org}$ excursions were distinguished on the basis of their age and changing trends and magnitudes of carbon isotope excursions, and can be correlated with those from the early Albian OAE 1b in Tethys, Pacific and North Atlantic.

(2) Three short-term episodes with mixed sources of terrestrial plants and lacustrine plankton, corresponding to the Kilian, Paquier and Leenhardt sub-events of OAE 1b, occurred in the context of increased pCO_2 and intensified continental weathering under warmer and more humid conditions during the early Albian OAE 1b interval. These episodes correlate with the high flux of nutrients and organic matter into lakes and thereby contributing to eutrophication and anoxia in lacustrine and in contemporaneous oceanic systems documented by previous workers.

Declaration of Competing Interest

The authors declare that they have no known competing financial interests or personal relationships that could have appeared to influence the work reported in this paper.

Acknowledgments

We thank Jason Hilton for discussion, Stephen Grasby and the other anonymous reviewers for constructive and helpful reviews of the manuscript. This study was supported by the Yue Qi Scholar Project of China University of Mining and Technology (Beijing), China; the National Natural Science Foundation of China (41572090; 42002128), and Shandong Key Laboratory of Depositional Mineralization & Sedimentary Mineral, Shandong University of Science and Technology, China (DMSM20190015).

Appendix A. Supplementary data

Supplementary data to this article can be found online at https://doi.org/10.1016/j.gsf.2021.101275.

References

Ando, A., Kakegawa, T., 2007. Carbon isotope records of terrestrial organic matter and occurrence of planktonic foraminifera from the Albian stage of Hokkaido, Japan: ocean-atmosphere $\delta^{13}C$ trends and chronostratigraphic implications. Palaios 22, 417–432. https://doi.org/10.2110/palo.2005.p05-104r.

Babechuk, M.G., Widdowson, M., Kamber, B.S., 2014. Quantifying chemical weathering intensity and trace element release from two contrasting basalt profiles, Deccan Traps, India. Chem. Geol. 363, 56–75. https://doi.org/10.1016/j.chemgeo.2013.10.027.

Barral, A., Gomez, B., Fourel, F., Daviero-Gomez, V., Lécuyer, C., 2017a. CO_2 and temperature decoupling at the million-year scale during the Cretaceous Greenhouse. Sci. Rep. 7, 8310. https://doi.org/10.1038/s41598-017-08234-0.

Barral, A., Gomez, B., Legendre, S., Lécuyer, C., 2017b. Evolution of the carbon isotope composition of atmospheric CO_2 throughout the Cretaceous. Palaeogeogr. Palaeoclimatol. Palaeoecol. 471, 40–47. https://doi.org/10.1016/j.palaeo.2017.01.034.

Benamara, A., Charbonnier, G., Adatte, T., Spangenberg, J.E., Föllmi, K.B., 2020. Precession-driven monsoonal activity controlled the development of the early Albian Paquier oceanic anoxic event (OAE 1b): Evidence from the Vocontian Basin, SE France. Palaeogeogr. Palaeoclimatol. Palaeoecol. 537, 109406. https://doi.org/10.1016/j.palaeo.2019.109406.

Bralower, T.J., Fullagar, P.D., Paull, C.K., Dwyer, G.S., Leckie, R.M., 1997. Mid-cretaceous strontium-isotope stratigraphy of deep-sea sections. Geol. Soc. Am. Bull. 109, 1421–1442. https://doi.org/10.1130/0016-7606(1997)109<1421:MCSISO>2.3.CO;2.

Bralower, T.J., CoBabe, E., Clement, B., Sliter, W.V., Osburn, C.L., Longoria, J., 1999. The record of global change in mid-Cretaceous (Barremian-Albian) sections from the Sierra Madre, Northeastern Mexico. J. Foramin. Res. 29 (4), 418–437.

Chen, F., Meng, X.Y., Ren, S.Q., Wu, C.L., 1988. The Early Cretaceous Flora of Fuxin Basin and Tiefa Basin, Liaoning Province. Geological Publishing House, Beijing, pp. 1–180 (in Chinese).

Coccioni, R., Sabatino, N., Frontalini, F., Gardin, S., Sideri, M., Sprovieri, M., 2014. The neglected history of Oceanic Anoxic Event 1b: insights and new data from the Poggio le Guaine section (Umbria-Marche Basin). Stratigraphy 11 (3–4), 245–282.

Coffin, M.F., Eldholm, O., 1994. Large igneous provinces: crustal structure, dimensions, and external consequences. Rev. Geophys. 32 (1), 1–36. https://doi.org/10.1029/93RG02508.

Cui, Y., Schubert, B.A., 2017. Atmospheric pCO_2 reconstructed across five early Eocene global warming events. Earth Planet. Sci. Lett. 478, 225–233. https://doi.org/10.1016/j.epsl.2017.08.038.

Dal Corso, J., Mills, B.J.W., Chu, D.L., Newton, R.J., Mather, T.A., Shu, W.C., Wu, Y.Y., Tong, J.N., Wignall, P.B., 2020. Permo-Triassic boundary carbon and mercury cycling linked to terrestrial ecosystem collapse. Nat. Commun. 11, 2962. https://doi.org/10.1038/s41467-020-16725-4.

Deng, S.H., Chen, F., 2001. The Early Cretaceous Filicopsida from Northeast China. Geological Publishing House, Beijing, pp. 1–249 (in Chinese).

Deng, S.H., Lu, Y.Z., Fan, R., Li, X., Fang, L.H., Liu, L., 2012. Cretaceous floras and biostratigraphy of China. J. Stratigr. 36 (2), 241–265.

Du, B.X., Sun, B.N., Zhang, M.Z., Yang, G.L., Xing, L.T., Tang, F.J., Bai, Y.X., 2016. Atmospheric palaeo-CO_2 estimates based on the carbon isotope and stomatal data of Cheirolepidiaceae from the Lower Cretaceous of the Jiuquan Basin, Gansu Province. Cretaceous Res. 62, 142–153. https://doi.org/10.1016/j.cretres.2015.07.020.

Erbachen, J., Gerth, W., Schmiedl, G., Hemleben, C.h., 1998. Benthic foraminiferal assemblages of late Aptian-early Albian black shale intervals in the Vocontian Basin. SE France. Cretaceous Res. 19 (6), 805–826.

Erbacher, J., Huber, B.T., Norris, R.D., Markey, M., 2001. Increased thermohaline stratification as a possible cause for an ocean anoxic event in the Cretaceous period. Nature 409 (6818), 325–327. https://doi.org/10.1038/35053041.

Erbacher, J., Thurow, J., Littke, R., 1996. Evolution patterns of radiolaria and organic matter variations: A new approach to identify sea-level changes in mid-Cretaceous pelagic environments. Geology 24 (6), 499–502.

Espitalié, J., Deroo, G., Marquis, F., 1985. La pyrolyse Rock-Eval et ses applications. Deuxiéme partie. Rev. Inst. Fr. Pet. 40, 755–784. https://doi.org/10.2516/ogst:1985035.

Espitalié, J., Laporte, J.L., Madec, M., Marquis, F., Leplat, P., Paulet, J., Boutefeu, A., 1977. Rapid method for source rocks characterization and for determination of petroleum potential and degree of evolution. Oil Gas Sci. Technol. 32 (1), 23–42.

Farquhar, G.D., Ehleringer, J.R., Hubick, K.T., 1989. Carbon isotope discrimination and photosynthesis. Ann. Rev. Plant Physiol. Plant Mol. Biol. 40, 503–537. https://doi.org/10.1146/annurev.pp.40.060189.002443.

Friedrich, O., Nishi, H., Pross, J., Schmiedl, G., Hemleben, C., 2005. Millenial- to centennial-scale interruptions of the oceanic anoxic event 1b (Early Albian, mid-Cretaceous) inferred from benthic repopulation events. Palaios 20, 64–77. https://doi.org/10.2110/palo.2003.p03-75.

Gao, Y., Wang, C.S., Hang, Y.J., Hu, B., 2017. Progress in the study of paleoclimate change in continental scientific drilling projects. Earth Sci. Front. 24 (1), 229–241 (in Chinese with English abstract).

Gao, Y., Wang, C., Wang, P., Gao, Y., Huang, Y., Zou, C., 2019. Progress on continental scientific drilling project of Cretaceous Songliao Basin (SK-1 and SK-2). Sci. Bull. 64 (2), 73–75. https://doi.org/10.1016/j.scib.2018.12.017.

Grasby, S.E., Sanei, H., Beauchamp, B., Chen, Z.H., 2013. Mercury deposition through the Permo-Triassic biotic crisis. Chem. Geol. 351, 209–216. https://doi.org/10.1016/j.chemgeo.2013.05.022.

Grasby, S.E., Them, T.R., Chen, Z., Yin, R., Ardakani, O.H., 2019. Mercury as a proxy for volcanic emissions in the geologic record. Earth-Sci. Rev. 196, 102880. https://doi.org/10.1016/j.earscirev.2019.102880.

Haworth, M., Hesselbo, S.P., McElwain, J.C., Robinson, S.A., Brunt, J.W., 2005. Mid-Cretaceous pCO_2 based on stomata of the extinct conifer Pseudofrenelopsis (Cheirolepidiaceae). Geology 33, 749. https://doi.org/10.1130/G21736.110.1130/2005137.

Herrle, J.O., 2002. Mid-Cretaceous paleoceanographic and paleoclimatologic implications on black shale formation of the Vocontian Basin and Atlantic: evidence from calcareous nannofossils and stable isotopes. Tübinger Mikropaläontologische Mitteilungen 27, 1–114.

Herrle, J.O., Kößler, P., Friedrich, O., Erlenkeuser, H., Hemleben, C., 2004. High-resolution carbon isotope records of the Aptian to Lower Albian from SE France and the Mazagan Plateau (DSDP Site 545): a stratigraphic tool for paleoceanographic and paleobiologic reconstruction. Earth Planet. Sci. Lett. 218 (1), 149–161. https://doi.org/10.1016/S0012-821X(03)00646-0.

Herrle, J.O., Pross, J., Friedrich, O., Kößler, P., Hemleben, C., 2003. Forcing mechanisms for mid-Cretaceous black shale formation: evidence from the Upper Aptian and Lower Albian of the Vocontian Basin (SE France). Palaeogeogr.

Palaeoclimatol. Palaeoecol. 190, 399–426. https://doi.org/10.1016/S0031-0182(02)00616-8.

Herrle, J.O., Schroder-Adams, C.J., Davis, W., Pugh, A.T., Galloway, J.M., Fath, J., 2015. Mid-cretaceous high arctic stratigraphy, climate, and oceanic anoxic events. Geology 43 (5), 403–406. https://doi.org/10.1130/G36439.1.

Hesselbo, S.P., Gröcke, D.R., Jenkyns, H.C., Bjerrum, C.J., Farrimond, P., Morgans Bell, H.S., Green, O.R., 2000. Massive dissociation of gas hydrate during a Jurassic oceanic anoxic event. Nature 406, 392–395. https://doi.org/10.1038/35019044.

Hong, S.K., Lee, Y.I., 2012. Evaluation of atmospheric carbon dioxide concentrations during the Cretaceous. Earth Planet. Sci. Lett. 327–328, 23–28. https://doi.org/10.1016/j.epsl.2012.01.014.

Hu, G., Hu, W., Cao, J., Yao, S., Liu, W., Zhou, Z., 2014. Fluctuation of organic carbon isotopes of the Lower Cretaceous in coastal southeastern China: Terrestrial response to the Oceanic Anoxic Events (OAE 1b). Palaeogeogr. Palaeoclimatol. Palaeoecol. 399, 352–362. https://doi.org/10.1016/j.palaeo.2014.01.027.

Hu, X.M., Jansa, L., Sarti, M., 2006. Mid-Cretaceous oceanic red beds in the Umbria-Marche Basin, central Italy: constraints on paleoceanography and paleoclimate. Palaeogeogr. Palaeoclimatol. Palaeoecol. 233 (3–4), 163–186. https://doi.org/10.1016/j.palaeo.2005.10.003.

Huang, Y.J., Wang, C.S., Gu, J., 2008. Cretaceous oceanic anoxic events: research progress and forthcoming prospects. Acta Geol. Sin. 82 (1), 21–30 (in Chinese with English abstract).

Huang, Q.H., Wu, H.C., Wan, X.Q., He, H.Y., Deng, C.L., 2011. New progress of integrated chronostratigraphy of the Cretaceous in Songliao Basin. J. Stratigr. 35 (3), 250–257 (in Chinese with English abstract).

Huber, B.T., Macleod, K.G., Gröcke, D.R., Kucera, M., 2011. Paleotemperature and paleosalinity inferences and chemostratigraphy across the Aptian/Albian boundary in the subtropical North Atlantic. Paleoceanography 26, PA4221. https://doi.org/10.1029/2011PA002178.

Jenkyns, H.C., 2010. Geochemistry of oceanic anoxic events. Geochem. Geophy. Geosy. 11 (3), 1–30. https://doi.org/10.1029/2009GC002788.

Jones, C.E., Jenkyns, H.C., 2001. Seawater strontium isotopes, oceanic anoxic events, and seafloor hydrothermal activity in the Jurassic and Cretaceous. Am. J. Sci. 301, 112–149. https://doi.org/10.2475/ajs.301.2.112.

Kohn, M.J., 2010. Carbon isotope compositions of terrestrial C_3 plants as indicators of (paleo)ecology and (paleo)climate. PNAS 107 (46), 19691–19695. https://doi.org/10.1073/pnas. http://dx.doi.org/1004933107/-/DCSupplemental.

Langford, F.F., Blanc-Valleron, M.-M., 1990. Interpreting Rock-Eval pyrolysis data using graphs of pyrolizable hydrocarbons vs. total organic carbon. AAPG Bull. 74 (6), 788–804. https://doi.org/10.1306/0C9B238F-1710-11D7-8645000102C1865D.

Larson, R.L., 1991. Geological consequences of superplumes. Geology 19 (10), 963–966. https://doi.org/10.1130/0091-7613(1991)019<0963:GCOS>2.3.CO;2.

Larson, R.L., Erba, E., 1999. Onset of the Mid-Cretaceous greenhouse in the Barremian-Aptian: igneous events and the biological, sedimentary, and geochemical responses. Paleoceanography 14 (6), 663–678.

Leavitt, S.W., 2009. Carbon isotopes, stable. In: Gornitz, V. (Ed.), Encyclopedia of Earth Sciences SeriesEncyclopedia of Paleoclimatology and Ancient Environments. Springer Netherlands, Dordrecht, pp. 133–136.

Leckie, R.M., Bralower, T.J., Cashman, R., 2002. Oceanic anoxic events and plankton evolution: biotic response to tectonic forcing during the mid-Cretaceous. Paleoceanography 17 (3), 11–13. https://doi.org/10.1029/2001PA000623.

Li, J.H., Jiang, H.F., 2013. Global Palaeoplate Reconstruction, Lithofacies Palaeogeography and Paleoenvironmental Atlas. Beijng: Geological Publishing House, pp. 1–127 (in Chinese).

Li, S.T., 1988. Fault Basin Analysis and Coal Accumulation. Geological Publishing House, Beijing, pp.1–367. (in Chinese).

Li, X.H., Wei, Y.S., Li, Y.X., Zhang, C.K., 2016. Carbon isotope records of the early Albian oceanic anoxic event (OAE) 1b from eastern Tethys (southern Tibet, China). Cretac. Res. 62, 109–121. https://doi.org/10.1016/j.cretres.2015.08.015.

Liu, J.Y., Wang, S.Y., Yin, J.H., 1992. Petroleum geological character of Fuxin Basin. Oil Gas Geol. 13 (4), 450–457 (in Chinese with English abstract).

Liu, Z.G., Chen, J.P., 1995. Coal-controlling structures in the Fuxin Basin. Geol. Rev. 41 (6), 499–502 (in Chinese with English abstract).

Lomax, B.H., Lake, J.A., Leng, M.J., Jardine, P.E., 2019. An experimental evaluation of the use of $\Delta^{13}C$ as a proxy for palaeoatmospheric CO_2. Geochim. Cosmochim. Acta 247, 162–174. https://doi.org/10.1016/j.gca.2018.12.026.

Ludvigson, G.A., Joeckel, R.M., Gonzalez, L.A., Gulbranson, E.L., Rasbury, E.T., Hunt, G. J., Kirkland, J.I., Madsen, S., 2010. Correlation of AptianeAlbian carbon isotope excursions in continental strata of the Cretaceous foreland basin, eastern Utah, U.S.A. J. Sed. Res. 80, 955–974. https://doi.org/10.2110/jsr.2010.086.

Ma, Y.S., Cui, S.Q., Wu, G.G., Wu, Z.H., Zhu, D.G., Li, X., Feng, X.Y., 2000. Uplift history of the Yiwulushan Mountains in West Liaoning. Acta Geosci. Sinica 21 (3), 245–253 (in Chinese with English abstract).

Miall, A.D., 2010. Alluvial deposits. In: James, N.P., Dairymple, R.W. (Eds.), Facies Models 4. Geological Association of Canada, St. John's, Canada, pp. 105–137.

McAnena, A., Flögel, S., Hofmann, P., Herrle, J.O., Griesand, A., Pross, J., Talbot, H.M., Rethemeyer, J., Wallmann, K., Wagner, T., 2013. Atlantic cooling associated with a marine biotic crisis during the mid-Cretaceous period. Nat. Geosci. 6 (7), 558–561. https://doi.org/10.1038/ngeo1850.

McElwain, J.C., Wade-Murphy, J., Hesselbo, S.P., 2005. Changes in carbon dioxide during an oceanic anoxic event linked to intrusion into Gondwana coals. Nature 435 (7041), 479–482. https://doi.org/10.1038/nature03618.

Mukhopadhyay, P.K., Wade, J.A., Kruge, M.A., 1995. Organic facles and maturation of Jurassic/Cretaceous rocks, and possible oil-source rock correlation based on pyrolysis of asphaltenes, Scotian Basin, Canada. Org. Geochem. 22 (1), 85–104. https://doi.org/10.1016/0140-6701(95)80171-5.

National Commission on Stratigraphy of China, 2014. Stratigraphic Chart of China 2014. Geological Publishing House, Beijing (in Chinese).

Navarro-Ramirez, J.P., Bodin, S., Heimhofer, U., Immenhauser, A., 2015. Record of Albian to early Cenomanian environmental perturbation in the eastern sub-equatorial Pacific. Palaeogeogr. Palaeoclimatol. Palaeoecol. 423, 122–137. https://doi.org/10.1016/j.palaeo.2015.01.025.

Nesbitt, H.W., Young, G.M., 1982. Early Proterozoic climates and plate motions inferred from major element chemistry of lutites. Nature 299 (5885), 715–717. https://doi.org/10.1038/299715a0.

Nguyen Tu, T.T., Kürschner, W.M., Schouten, S., Van Bergen, P.F., 2004. Leaf carbon isotope composition of fossil and extant oaks grown under differing atmospheric CO_2 levels. Palaeogeogr. Palaeoclimatol. Palaeoecol. 212 (3-4), 199–213. https://doi.org/10.1016/j.palaeo.2004.05.023.

Park, R., Epstein, S., 1960. Carbon isotope fractionation during photosynthesis. Geochim. Cosmochim. Acta 21 (1-2), 110–126. https://doi.org/10.1016/S0016-7037(60)80006-3.

Parker, A., 1970. An index of weathering for silicate rocks. Geol. Mag. 107 (6), 501–504.

Pepper, A.S., Corvi, P.J., 1995. Simple kinetic models of petroleum formation. Part I: oil and gas generation from kerogen. Mar. Petrol. Geol. 12 (3), 291–319. https://doi.org/10.1016/0264-8172(95)98381-E.

Pross, J., 2001. Paleo-oxygenation in Tertiary epeiric seas: evidence from dinoflagellate cysts. Palaeogeogr. Palaeoclimatol. Palaeoecol. 166 (3-4), 369–381. https://doi.org/10.1016/S0031-0182(00)00219-4.

Robinson, S.A., Heimhofer, U., Hesselbo, S.P., Petrizzo, M.R., 2017. Mesozoic climates and oceans — a tribute to Hugh Jenkyns and Helmut Weissert. Sedimentology 64, 1–15. https://doi.org/10.1111/sed.12349.

Sabatino, N., Coccioni, R., Manta, D.S., Baudin, F., Vallefuoco, M., Traina, A., Sprovieri, M., 2015. High-resolution chemostratigraphy of the late Aptian-early Albian oceanic anoxic event (OAE 1b) from the Poggio le Guaine section (Umbria–Marche Basin, central Italy). Palaeogeogr. Palaeoclimatol. Palaeoecol. 426, 319–333. https://doi.org/10.1016/j.palaeo.2015.03.009.

Sabatino, N., Ferraro, S., Coccioni, R., Bonsignore, M., Del Core, M., Tancredi, V., Sprovieri, M., 2018. Mercury anomalies in upper Aptian-lower Albian sediments from the Tethys realm. Palaeogeogr. Palaeoclimatol. Palaeoecol. 495, 163–170. https://doi.org/10.1016/j.palaeo.2018.01.008.

Schlanger, S.O., Jenkyns, H.C., 1976. Cretaceous oceanic anoxic events: causes and consequences. Geol. Mijnbouw 55 (3–4), 179–184.

Schubert, B.A., Jahren, A.H., 2012. The effect of atmospheric CO_2 concentration on carbon isotope fractionation in C_3 land plants. Geochim. Cosmochim. Acta 96, 29–43. https://doi.org/10.1016/j.gca.2012.08.003.

Schubert, B.A., Jahren, A.H., 2013. Reconciliation of marine and terrestrial carbon isotope excursions based on changing atmospheric CO_2 levels. Nat. Commun. 4 (1), 1–17. https://doi.org/10.1038/ncomms2659.

Shen, J., Chen, J.B., Algeo, T.J., Yuan, S.L., Feng, Q.L., Yu, J.X., Zhou, L., O'Connell, B., Planavsky, N.J., 2019. Evidence for a prolonged Permian-Triassic extinction interval from global marine mercury records. Nat. Commun. 10, 1563. https://doi.org/10.1038/s41467-019-09620-0.

Skelton, P.W., 2003. The Cretaceous World. Cambridge University Press, London, pp. 1–350.

Sláma, J., Košler, J., Condon, D.J., Crowley, J.L., Gerdes, A., Hanchar, J.M., Horstwood, M.S.A., Morris, G.A., Nasdala, L., Norberg, N., Schaltegger, U., Schoene, B., Tubrett, M.N., Whitehouse, M.J., 2008. Plešovice zircon — A new natural reference material for U-Pb and Hf isotopic microanalysis. Chem. Geol. 249 (1–2), 1–35. https://doi.org/10.1016/j.chemgeo.2007.11.005.

Su, N., Zhu, G., Wu, X.D., Yin, H., Lu, Y.C., Zhang, S., 2021. Back-arc tectonic tempos: Records from Jurassic-Cretaceous basins in the eastern North China Craton. Gondwana Res. 90, 241–257. https://doi.org/10.1016/j.gr.2020.12.002.

Sun, W.L., 2006. China Coalbed Methane Basins Atlas. Geological Publishing House, Beijing, pp. 1–233 (in Chinese).

Sun, Y., Li, X., Zhao, G., Liu, H., Zhang, Y., 2016. Aptian and Albian atmospheric CO_2 changes during oceanic anoxic events Evidence from fossil Ginkgo cuticles in Jilin Province, Northeast China. Cretaceous Res. 62, 130–141. https://doi.org/10.1016/j.cretres.2015.12.007.

Trabucho Alexandre, J., van Gilst, R.I., Rodríguez-López, J.P., De Boer, P.L., 2011. The sedimentary expression of oceanic anoxic event 1b in the North Atlantic. Sedimentology 58, 1217–1246. https://doi.org/10.1111/j.1365-3091.2010.01202.x.

Tsikos, H., Karakitsios, V., van Breugel, Y., Walsworth-Bell, B., Bombardiere, L., Petrizzo, M.R., Damst, J.S.S., Schouten, S., Erba, E., Silva, I.P., Farrimond, P., Tyson, R.V., Jenkyns, H.C., 2004. Organic-carbon deposition in the cretaceous of the Ionian Basin, NW Greece: the Paquier Event (OAE 1b) revisited. Geol. Mag. 141 (4), 401–416. https://doi.org/10.1017/S0016756804009409.

Vandenbroucke, M., Largeau, C., 2007. Kerogen origin, evolution and structure. Org Geochem. 38 (5), 719–833. https://doi.org/10.1016/j.orggeochem.2007.01.001.

Wagner, T., Wallmann, K., Herrle, J.O., Hofmann, P., Stuesser, I., 2007. Consequences of moderate ~25,000 yr lasting emission of light CO_2 into the mid-Cretaceous ocean. Earth Planet. Sci. Lett. 259 (1–2), 200–211. https://doi.org/10.1016/j.epsl.2007.04.045.

Wan, X.Q., Li, G., Huang, Q.H., Xi, D.P., Chen, P.J., 2013. Division and correlation of terrestrial Cretaceous stages in China. J. Stratigr. 37 (4), 457–471 (in Chinese with English abstract).

Wan, X.Q., Wu, H.C., Xi, D.P., Liu, M.Y., Qin, Z.H., 2017. Terrestrial biota and climate during Cretaceous greenhouse in NE China. Earth Sci. Front. 24 (1), 18–31 (in Chinese with English abstract).
Wang, C.S., 2006. Coupling of the earth surface system: inferring from the Cretaceous major geological events. Adv. Earth Sci. 21 (7), 838–842 (in Chinese with English abstract).
Wang, C.S., Hu, X.M., Sarti, M., Scott, R.W., Li, X.H., 2005. Upper Cretaceous oceanic red beds in southern Tibet: a major change from anoxic to oxic, deep-sea environments. Cretac. Res. 26 (1), 21–32. https://doi.org/10.1016/j.cretres.2004.11.010.
Wang, W.F., Lu, S.K., Guo, Y.X., Sun, Y.P., 1998. Tectonic geometry and type of traps in Fuxin Basin. J. Univ. Petrol. China 22 (3), 29–33 (in Chinese with English abstract).
Weissert, H., Lini, A., 1991. Ice age interludes during the time of Cretaceous greenhouse climate. In: Mueller, D.W., McKenzie, J.A., Weissert, H. (Eds.), Controversies in Modern Geology. Academic Press, London, pp. 173–191.
Wiedenbeck, M., Allé, P., Corfu, F., Griffin, W.L., Meier, M., Oberli, F., Vonquadt, A., Roddick, J.C., Spiegel, W., 1995. Three natural zircon standards for U-Th-Pb, Lu-Hf, trace-element and Ree analyses. Geostand. Newsl. 19 (1), 1–23.
Wiedenbeck, M., Hanchar, J.M., Peck, W.H., Sylvester, P., Valley, J., Whitehouse, M., Kronz, A., Morishita, Y., Nasdala, L., Fiebig, J., Franchi, I., Girard, J.-P., Greenwood, R.C., Hinton, R., Kita, N., Mason, P.R.D., Norman, M., Ogasawara, M., Piccoli, P.M., Rhede, D., Satoh, H., Schulz-Dobrick, B., Skår, O., Spicuzza, M.J., Terada, K., Tindle, A., Togashi, S., Vennemann, T., Xie, Q., Zheng, Y.F., 2004. Further characterisation of the 91500 zircon crystal. Geostand. Geoanal. Res. 28 (1), 9–39.
Wu, F.Y., Xu, Y.G., Zhu, R.X., Zhang, G.W., 2014. Thinning and destruction of the cratonic lithosphere: a global perspective. Sci. China Earth Sci. 57 (2), 2878–2890. https://doi.org/10.1007/s11430-014-4995-0.
Xi, D.P., Wan, X.Q., Li, G.B., Li, G., 2019. Cretaceous integrative stratigraphy and timescale of China. Sci. China Earth Sci. 62 (1), 256–286. https://doi.org/10.1007/s11430-017-9262-y.
Xu, X.T., Shao, L.Y., Lan, B., Wang, S., Hilton, J., Qin, J.Y., Hou, H.H., Zhao, J., 2020a. Continental chemical weathering during the Early Cretaceous Oceanic Anoxic Event (OAE 1b): a case study from the Fuxin fluvio-lacustrine basin, Liaoning Province, NE China. J. Palaeogeogr. 9 (2), 246–266. https://doi.org/10.1186/s42501-020-00056-y.
Xu, X.T., Shao, L.Y., Fu, Y.F., Wang, D.D., Cai, H.A., Qin, J.Y., Hou, H.H., Zhao, J., 2020b. Sequence palaeogeography, lacustrine basin evolution, and coal accumulation in the Lower Cretaceous Fuxin continental faulted basin, China. Geol. J. 55 (2), 1195–1215. https://doi.org/10.1002/gj.3483.
Yevenes, M.A., Lagos, N.A., Farías, L., Vargas, C.A., 2019. Greenhouse gases, nutrients and the carbonate system in the Reloncaví Fjord (Northern Chilean Patagonia): Implications on aquaculture of the mussel, Mytilus chilensis, during an episodic volcanic eruption. Sci. Total Environ. 669, 49–61. https://doi.org/10.1016/j.scitotenv.2019.03.037.
Zhang, F.Q., Chen, H.L., Yu, X., Dong, C.W., Yang, S.F., Pang, Y.M., Batt, G.E., 2011. Early Cretaceous volcanism in the northern Songliao Basin, NE China, and its geodynamic implication. Gondwana Res. 19, 163–176. https://doi.org/10.1016/j.gr.2010.03.011.
Zhang, H., Liu, X.M., Li, Z.T., Yang, F.L., Wang, X.R., 2005. Early Cretaceous large-scale Crustal thinning in the Fuxin-Yixian basin and adjacent area in western Liaoning. Geol. Rev. 51 (4), 360–372 (in Chinese with English abstract).
Zhou, Z., Barrett, P.M., Hilton, J., 2003. An exceptionally preserved Lower Cretaceous ecosystem. Nature 421, 807–814. https://doi.org/10.1038/nature01420.
Zhu, R., Zhang, H., Zhu, G., Meng, Q., Fan, H., Yang, J., Wu, F., Zhang, Z., Zheng, T., 2017. Craton destruction and related resources. Int. J. Earth Sci. 106, 2233–2257. https://doi.org/10.1007/s00531-016-1441-x.
Zhu, Z.M., Yan, J.F., Shen, B., Zhou, J.Y., 2007. Co-existing formation of multi-energy resources in the Fuxin Basin analysis from tectonic-thermal events. Adv. Earth Sci. 22 (5), 468–479 (in Chinese with English abstract).
Zhu, Z.Y., Jiang, S.Y., Liu, G.X., Zhao, K.D., 2013. Precise dating of the Middle Permian: Zircon U-Pb geochronology from volcanic ash beds in the basal Gufeng Formation, Yangtze region, South China. Gondwana Res. 23, 1599–1606. https://doi.org/10.1016/j.gr.2012.08.008.